Telomere-driven replicative crisis is driven by large-scale changes in genomic architecture

Kate Liddiard, Emmon Coral, Harsh Bhatt, et al.

Genome Res. published online June 29, 2026
Access the most recent version at doi:10.1101/gr.281373.125

Telomere-driven replicative crisis is driven by large-scale changes in genomic architecture

Authors: Kate Liddiard[1*], Emmon Coral[1], Harsh Bhatt[1], Kez Cleal[1] and Duncan M. Baird[1]

[1]Division of Cancer and Genetics, School of Medicine, Cardiff University, Heath Park, Cardiff, United Kingdom, CF14 4XN.

*Requests for further information and resources should be directed to and will be fulfilled by the lead contact, Kate Liddiard: liddiardk@cardiff.ac.uk

Running title: Genome instability and structural variation in replicative crisis

Abstract

Telomere-driven replicative crisis transforms the architecture of the evolving cancer genome, yet the mechanisms and consequences remain incompletely resolved, with potential biomarkers undiscovered. To address this, we have employed novel tools and methodologies to explore a human fibroblast model of crisis using high resolution multi-omics analyses. We have developed a unique chromatin conformation capture procedure for identifying distant genomic loci that interact with eroding telomeres, uncovering large-scale structural changes that accompany crisis transition. We reveal the remarkable shift from local to distant genomic interactions consistent with crisis-induced chromatin decompaction and altered gene expression. To resolve variation within challenging repetitive sequences disclosed in the complete telomere-to-telomere human reference, we designed a targeted capture panel, uncovering ageing signatures within centromeric sequences and gross copy number losses within ribosomal DNA tracks and near to the chromosome ends. We have employed both short- and long-read sequencing of purified extrachromosomal circular DNA to expose an unequivocal transition in the abundance, complexity and sequence content of these sporadic structural variants during crisis. By integrating parallel sequencing datasets, we provide a multifaceted characterisation of replicative crisis in unprecedented detail. Our findings demonstrate that telomere dysfunction and transcription-driven chromatin reorganisation combine to connect replication stress to telomere fusions, eccDNA emergence and genome instability, generating dynamic biomarkers of cellular stress relevant to cancer progression.

Introduction

Telomere-driven replicative crisis is characterised by the fusion of eroded and damaged telomeres that can precipitate genomic instability through breakage-fusion-bridge cycles (McClintock 1941) in the context of unchecked cellular proliferation. This volatility is fundamental to malignant transformation (Counter et al. 1992), facilitating the emergence of oncogenic genome recombinations, including those capacitating telomere length (TL) maintenance and cellular immortality (Kim et al. 1994). The crisis state can be modelled in human fibroblasts through the transgenic expression of human papillomavirus 16 (HPV16) *E6* and *E7* oncogenes that suppress endogenous RB1 and TP53 activity, concurrently attenuating cell cycle checkpoints and stimulating cell cycle progression (Shay et al. 1991; Bond et al. 1999). This results in an extended replicative lifespan, accompanied by aberrant genomic recombinations and inflammatory signalling (Nassour et al. 2019). Since telomere fusions are rare in cells with stable genomes (Capper et al. 2007), their detection can be associated with cancer prognosis (Lin et al. 2010; Simpson et al. 2015). Each individual telomere fusion constitutes a unique genome recombination, so the development of clinical assays will be dependent on the resolution of universal mechanisms or recurrent foci.

The critical contribution of subnuclear architecture to malignancy has been increasingly appreciated with the advent of technologies for the capture and sequence-based determination of chromatin interactions (Dekker et al. 2002; Lieberman-Aiden et al. 2009; Downes et al. 2022). Structural variants (SV; including telomere fusions) represent both causal agents and consequences of altered chromatin architecture (Dubois et al. 2022). Mutations in chromatin loop anchors have been implicated in oncogenesis, leading to juxtaposition of ordinarily segregated loci (Khoury et al. 2020). These shifts in genomic organisation both increase the probability of recombination (Sachs et al. 1997; Lin et al. 2009) between distant loci and provide opportunities for altered gene regulation through aberrant contact with enhancer or insulator sequences (Ryan et al. 2015). Enhancer hijacking (Northcott et al. 2014) is a recognised mode of oncogene activation and influence whereby inappropriate connections between regulatory sequences and gene promoters drives expression of genes that confer a survival or replicative advantage. Conversely, chromosome translocations can disrupt Topologically associating domain (TAD) boundaries (Dixon et al. 2012) or the proper compartmentalisation of chromatin, deranging DNA repair (Lemaître et al. 2014) and replication (Whalen et al. 2020). Drastic alterations in chromosome contacts can be observed in cancer cells, underpinning the malignant phenotype (Fritz et al. 2014; Hung et al. 2021).

Double-strand DNA breaks (DSB) are prerequisites for SV formation as effectors of replication fork stalling and substrates of DNA repair. Gene transcription (Williamson and Lees-Miller 2011; Fong et al. 2013) and DNA replication (Xu et al. 2011; Saxena and Zou 2022) are the prevalent sources of endogenous DSB, associating both active genes and late-replicating repetitive sequences with mutagenic processes. The coordination of these processes and natural phasing with the cell cycle also contributes to unusual and potentially deleterious long-range interactions. DSB processing results in elevated DNA mobility (Miné-Hattab and Rothstein 2012; Cho et al. 2014; Lottersberger et al. 2015) and relocalisation of both coding (Penzo et al. 2023) and repetitive sequences (Khadaroo et al. 2009) to the nuclear periphery (Oza et al. 2009; Freudenreich and Su 2016) may further expedite aberrant interactions (Larizza and Colombo 2024), including telomere fusions (Liddiard et al. 2016, 2021). Persistent DNA damage contributes to replication stress that may result in the aberrant recombination of distant sites that share replication timing through a template-switching mechanism (Arlt et al. 2009; Zhang et al. 2009; Böhly et al. 2022).

Extrachromosomal circular DNA (eccDNA) represent SV that are detached from the linear genome and able to replicate independently of the cell cycle (Jaworski et al. 2025). As such, they may have serious consequences for gene copy number and transcriptional outputs, as well as subclonal heterogeneity. Since DNA circles capture regulatory as well as coding sequences and have the capacity to spatially cluster in hubs (Hung et al. 2021), their influence can extend over entire signalling networks (Hung et al. 2024). Furthermore, their detachment from chromosomal organisation licences the activation of formerly silenced loci, including transposable elements (Kraft et al. 2025) and enhancers (Mortenson et al. 2024). Large eccDNA (including double minutes) bearing oncogenic coding sequences are closely associated with genome instability and poor prognosis amongst cancer patients (Kim et al. 2020; Luo et al. 2022; Yan et al. 2024). Recurrent events characterise particular cancers, such as the amplification of *EGFR* in glioma (Sauter et al. 1996) and *ERBB2* in breast cancer (Vicario et al. 2015), offering opportunities for novel diagnostics (Hung et al. 2022; Behrouzi et al. 2025) and therapeutics (Von Hoff et al. 1992; Shimizu et al. 2007).

Although the oncogenic impact of large eccDNA is well-recognised (Luo et al. 2022; Peng et al. 2022), there exist multiple different species of varying sizes and stability, generated by diverse cellular processes (Yang et al. 2022) that overlap with those implicated in SV formation (Zhou et al. 2024). The detection of eccDNA in healthy (Møller et al. 2016, 2018) as well as cancerous cells (Kumar et al. 2020; Tatman and Black 2022) affirms the formation of at least subsets of these events as byproducts of constitutive processes including transcription, replication, DNA repair and

apoptosis. A classification system based on size, DNA content and pathogenic effects has been proposed (Zhou et al. 2024), yet functional stratification remains constrained by limited studies of eccDNA heterogeneity in cancer. In particular, the intracellular localisation (Kanda et al. 2001; Schenkel et al. 2023), degradation (Qiu et al. 2021), immunogenicity (Wu et al. 2024b) and capacity for re-integration into the linear genome (Alitalo et al. 1983; Vogt et al. 2014) of these different eccDNA species is incompletely understood with respect to cellular function and transformation. However, accumulation in ageing tissue in accordance with replication stress, genome instability and inflammation recommends eccDNA as biomarkers of disease even where recurrent or high copy number events cannot be identified.

In this study, we sought to disentangle the relative contributions of telomere attrition, replication stress, genome instability and SV formation to the evolution of the cancer genome and phenotype. Because these processes are typically investigated in isolation, their interdependencies and shared genomic contexts remain poorly defined. We therefore designed a multi-modal sequencing strategy to enable integrated analyses across genomic features, spatial contexts and variant classes, with the aim of identifying common patterns and mechanisms that could inform the rational development of future diagnostic assays and therapeutic strategies.

Results

Multiomics profiling of telomere-driven replicative crisis in human fibroblasts

We previously reported a correspondence between genes differentially-expressed and recombined with telomeres during replicative crisis in human fibroblasts (Liddiard et al. 2021). To uncover the mechanisms by which eroded telomeres become juxtaposed with transcribed genes and the consequences of altered long-range chromosomal interactions, we performed multi-modal sequencing of HPV16 *E6E7* transformed MRC5 cells (Figure 1A) transiting replicative crisis (Supplemental Figure S1A). Since replicative crisis is triggered by telomere dysfunction (Capper et al. 2007), we defined 'Early', 'Deep' and 'Late' crisis time points according to the emergence of telomere fusions in our MRC5^{E6E7} model (Supplemental Figure S1B). In most experiments, an 'Early' (23 Population Doublings [PD]) MRC5^{E6E7} sample was compared with a 'Deep' (PD47) crisis-stage sample (Supplemental Figure S1A) that exhibited greater abundance of telomere fusions at multiple chromosome ends (Supplemental Figure S1B), associated with shortened telomere length (Supplemental Figure S1C). These sampling points were selected to elucidate DNA structural and organisational transitions independent of cellular proliferative capacity, volume and viability (Supplemental Figure S1D) that are compromised in late crisis and senescence (Mitsui and Schneider 1976; Neurohr et al. 2019; Liddiard et al. 2021). For extrachromosomal circular DNA (Circle-Seq) sequencing (Figure 1A) baseline genomic information was critical to the interpretation of crisis-mediated effects and was provided by sampling of 'Untransformed' MRC5. For targeted capture genome instability assays, a terminal 'Late' (PD57) crisis MRC5^{E6E7} sample was also included for more comprehensive longitudinal comparisons.

Chromatin capture (Capture-C) (Downes et al. 2022, 2023) was performed using probes specific for Chr17p (17pT) and ChrXpYp (XpT) telomere-adjacent sequences, as well as an intergenic internal ChrXpYp (XpG) control locus (Supplemental Figure S2) to characterise the diversification of telomere contacts in crisis. Circle-Seq (Møller 2020) (Supplemental Figure S3) was employed to distinguish eccDNA produced in 'normal' compared with transformed cells and determine interrelationships with telomere fusions and gross karyotypic changes. KAS-seq (Lyu et al. 2022) was used to colocalise sites of DNA replication, transcription and repair with SV identified through parallel sequencing processes. Targeted capture experiments were conducted across the whole range of MRC5 samples to explore potentially unstable sequences under the pressure of crisis and their associations with telomere dysfunction.

These related datasets were analysed for recurrent locations and features informative of the origins and effectors of genomic variation (Figure 1Bi). Sequence context proved a potent classifier, resulting in clear sample segregation by crisis stage and underlying vulnerabilities (Figure 1Bii; Supplemental Figure S4). Specifically, telomere fusions clustered with eccDNA and late crisis chromatin capture datasets, suggesting common mechanisms driving genomic rearrangements.

Single-strand DNA peaks outline transcriptional networks and crisis-induced replication stress

Investigating the impact of DNA damage (KAS-seq) for chromatin remodelling, we realised a correspondence between single strand DNA (ssDNA) signal peaks and coding sequence (Figure 2Ai) irrespective of crisis stage. Using our crisis cell RNA-seq data (Liddiard et al. 2021), we were able to corroborate the active expression of these genes within MRC5^{E6E7} cells. Compared with a dataset derived from 1 million random genomic coordinates (generated using BEDTools RandomBED (Quinlan and Hall 2010; Galaxy Community 2024)), ssDNA peaks called from discrete crisis samples exhibited substantially higher proportions of genomic intervals overlapping with genes and expressed genes (Figure 2Aii). Only the ssDNA peaks detected throughout crisis ('Shared' between datasets) displayed significant association with R-loops (Supplemental Figure S4), suggesting that, whilst unique ssDNA peaks demarcate stage-specific transcription, common peaks likely represent sites of replication stress or transcription-replication clashes. Whereas the Early crisis ssDNA peaks dataset (2455 genes) was enriched for genes involved in biogenesis and proliferation (Supplemental Figure S5A), the Deep crisis dataset (2001 genes) evidenced the inflammation that accompanies persistent DNA damage and cellular stress (Nassour et al. 2019; Lex et al. 2020; Dust et al. 2022; Gulen et al. 2023). Genes bearing ssDNA marks at both crisis stages ('Shared'; 1668 genes) were typically longer genes (Supplemental Figure S5B) more predisposed to replication errors (Wei et al. 2016; Berkemeier et al. 2025). Global transcription declined with crisis transition (Supplemental Figure S5C), but this was insignificant for genes closer to the telomeres with lower mean lengths (Supplemental Figure S5D). Consonantly, ssDNA peaks in Deep crisis marked shorter genes (Supplemental Figure S5B) closer to the chromosome termini (Supplemental Figure S5E), affirming telomere-proximal gene expression accompanying telomere attrition (Baur et al. 2001).

Ascribing KAS-seq signal peaks to 5' or 3' gene locations revealed a compelling reduction in ssDNA peaks overlapping transcription start sites (TSS) in Deep crisis (Figure 2B) and corresponding elevation in 3' DNA damage characteristic of replication fork stalling and structural instability (Li and Manley 2005; Gadgil et al. 2020, 2024; Stoy et al. 2023).

We observed increased incidence of G4-quadruplex, mirror and short tandem repeat motifs downstream of genes with 3' ssDNA peaks in Deep crisis (Figure 2C), proposing these structures as conducive to DNA lesions and replication stress in crisis (Makova and Weissensteiner 2023; Gadgil et al. 2024). Thus, KAS-seq signal peaks may be adopted as surrogate markers of both active transcription and potential sources of replication fork stalling in replicative crisis.

Crisis reshapes the 3-dimensional (3D) genome

Telomere fusions amplified from MRC5^{E6E7} displayed progressively increasing proportions of longer-range inter- than intra-chromosomal telomere-telomere rearrangements (Figure 3A) with crisis transition. Conversely, the incidence of telomere-telomere (both intra- and inter-) fusions in Early crisis samples was far lower than stochastic genomic rearrangements, likely reflecting the more limited reservoir of eroded and fusogenic telomeres at this stage. Telomere-genomic recombinations may occur in the absence of telomere erosion through synapsis of DSB in both locations. To understand the differential interactions of functional and eroded telomeres and their potential contributions to malignant recombination, (Figure 3B; Supplemental Figure S6A, S6B), we performed chromatin capture (Capture-C) in Early and Deep crisis MRC5^{E6E7} using Chr17p (17pT) and ChrXp (XpT) telomere-adjacent capture probes and a non-telomeric control probe (XpG) (Figure 3C; Supplemental Figure S2).

We observed robust elevations in long-range (trans) interactions (Figure 4Ai) from both telomere-adjacent (17pT and XpT) and genomic (XpG) capture probes (but not unrelated capture probes targeting 5 distinct genes; Supplemental Figure S6C) with advancing crisis. This cis to trans shift was accentuated by a pronounced increase in centromeric contacts (Figure 4Aii, 4Aiii) and a complementary suppression of telomere-proximal connections (Figure 4Aiv), potentially linked to telomere shortening (Supplemental Figure S1) (Baur et al. 2001).

Subsets of genes interacting with telomere-adjacent probes were conjointly detected as telomere fusions in crisis MRC5^{E6E7} (Figure 4B), suggesting recombination is, in part, related to the probability of stochastic contact between distant sites. Gene overlaps were functionally enriched in transmembrane signalling networks (Supplemental Figure S6D) critical to the DNA damage response (DDR) (Maliszewska-Olejniczak and Bednarczyk 2024), indicating that genomic rearrangements incorporate genes actively expressed and required for crisis cell viability. This creates a potential liability, whereby ongoing expression and reliance on these pathways increases the likelihood that further rearrangement or mutation compromises essential cellular processes. Intersections between Capture-C datasets and

genes expressed by crisis MRC5^{E6E7} cells were consistently lower than for our collection of MRC5^{E6E7} telomere fusions but exhibited marked probe-dependent effects (Figure 4C). Thus, transcription is less explicitly associated with subtelomere interactions than fusions. Underlying associations with DNA repeat classes revealed only a dominance of LINE repeats at captured sites, with reductions in SINE and satellite sequences observed for all probes (Figure 4D) in Deep crisis. Reassuringly, we detected no spurious enrichment of LTR sequences despite the prominence of these repeats at the chromosome ends (Figure 3C).

Exploring the totality of Capture-C gene contacts, we found Deep crisis subtelomere interactions to be specifically enriched in sodium transport genes (Supplemental Figure S7A) and so we queried The ICGC/TCGA Pan-cancer database (ICGC/TCGA Pan-Cancer Analysis of Whole Genomes Consortium 2020) for cognate gene abnormalities in cancer patients. We discovered aberrations in 70% patients (1808 of 2583 patients sampled), with amplifications being the most prevalent (Supplemental Figure S7B). Variations in 6 of these genes (Supplemental Figure S7C) had significant impact for patient survival, linking the altered chromatin configurations we observed during crisis transition with cancer progression.

MRC5 cells have ChrXpYp alleles with disparate telomere lengths (Supplemental Figure S1C), enabling the longer (A) and shorter (B) alleles to be distinguished through heterozygous single nucleotide polymorphisms in the telomere-adjacent DNA (Baird et al. 1995). This allelic asymmetry allows telomere length-dependent effects on long-range subtelomeric interactions to be assessed independently of crisis stage or replicative age, as both long and short telomere alleles can be simultaneously tracked within the same crisis cells. The shorter telomere (B) allele contributed to the greater proportion of intra-chromosomal interactions throughout crisis than the longer telomere (A) allele (Figure 4E), whereas no differential inter-chromosomal association was discerned. Both alleles echoed the diminished telomere-proximal contacts in Deep crisis (Supplemental Figure S8A) observed with the wider datasets (Figure 4Aiv), but only a robust association between the long allele and centromeres at the same stage (Supplemental Figure S8B). Overall, the shorter (B) telomere allele displayed elevated intersections with expressed genes (Figure 4Fi) and SINE repeats (Figure 4Fii; Supplemental Figure 8C) in contrast to the longer (A) telomere allele that had proportionally more interactions with centromere satellite (CenSat) and satellite repeats. These observations infer compartmentalisation of extended repeat tracts within the nucleus, abrogated by telomere shortening that confers extraordinary mobility (Cho et al. 2014) and capacitates fusion with sister chromatids and

genomic DSB (Liddiard et al. 2016). The increased mean lengths of genes captured in Deep crisis (Figure 4Gi) or with the shorter B allele (Figure 4Gii) is consistent with longer genes precipitating replication stress (Wei et al. 2016) and DSB that promote co-segregation with deprotected telomeres. These results also corroborate recent findings of allele-specific chromatin organisation (Irastorza-Azcarate et al. 2025).

We performed XSTREME motif discovery and enrichment analysis (Bailey 2021) in sequences flanking Capture-C probe interactions with genes also disrupted by telomere fusions (Figure 4C) to identify organising factors (Supplemental Figure S9). Binding sites for chromatin insulator loop factors (including ZNF770, ZNF335, ZFX and PITX2) (Trieu et al. 2020) were amongst the most enriched motifs, pinpointing topological boundaries as sites of particular vulnerability in the evolving crisis genome. Binding motifs for the inflammatory modulators BCL6 (Sawant et al. 2012) and EGR3 (Baron et al. 2015; Ogbe et al. 2015) were exclusively enriched in sequence overlaps with the telomere-adjacent capture probes and not XpG or coding sequence probes. RNA-seq and KAS-seq data confirmed expression of *BCL6* and *EGR3* genes in MRC5^{E6E7} cells, propounding crisis-activated transcription (and the consequential disruption of this) as being instrumental in stress-induced genome reorganisation (Dimitrova et al. 2008; Baron et al. 2015; Cardenas et al. 2017; Arnould et al. 2023).

Cellular stress drives a shift in extrachromosomal circular DNA profiles

Telomere fragments (Lovejoy et al. 2012; Geiller et al. 2022) and telomere fusions (Muyas et al. 2024) have been detected as circular DNA species and so we next sought to clarify the interrelationship between telomere dysfunction and these specialised SV. To ascertain the hierarchy and salient features of events (Tatman and Black 2022),

we first purified, amplified and sequenced eccDNA (Møller et al. 2016; Møller 2020; Chen et al. 2022) from Early and Deep crisis MRC5^{E6E7} fibroblasts, as well as the parental Untransformed cells (Supplemental Figure S3). The chromosomal locations of all eccDNA junctions sequenced in four independent experiments are displayed in Figure 5A and Supplemental Figure S10A and enumerated in Supplemental Table S1. Contrary to the high copy number DNA circles serving as oncogenic drivers of specific cancers (Schwab et al. 1983; Sauter et al. 1996), we did not identify breakpoints common to replica samples (Yi et al. 2022), advocating transient and labile eccDNA formation resemblant of the unique telomere fusions that arise during crisis (Liddiard et al. 2016). Furthermore, the eccDNA we sequenced contained both coding and intergenic sequences, rather than entire genes and varied in length from hundreds to millions of base-pairs, affirming the capture of diverse eccDNA species (Yang et al. 2022).

Consonant with the increased abundance of eccDNA amplified from MRC5 progressing deeper into replicative crisis (Supplemental Figure S3Biii), we measured escalations in both mean eccDNA sizes (Figure 5B) and complexity (Figure 5C). Long-read sequencing revealed a substantial expansion in the proportion of eccDNA comprising DNA translocations for the Deep crisis samples that mirrors the increasing disorganisation of the crisis genome (Cleal et al. 2019) and the enhanced capacity for long-range interactions (Figure 4A). Thus, eccDNA derived from Untransformed cells are evidently distinct from those detected in transformed MRC5^{E6E7} cells. Indeed, intersections across datasets demonstrated that both the overall eccDNA profiles (Supplemental Figure S10B) and genes captured within eccDNA (Figure 5Di) showed greater concordance between Early and Deep crisis than between Untransformed samples and either crisis stage.

Although eccDNA were smaller in Untransformed cells than crisis cells (Figure 5B), the genes within the genomic intervals from which they originated had longer mean lengths (Figure 5Dii), suggesting that intermediates of late-replication may circularise during normal cell division (Møller et al. 2018; Berkemeier et al. 2025; Eugen-Olsen et al. 2025). Functional enrichments in related gene networks (cell junctions and transmembrane signalling) were determined for both direct overlaps (Figure 5Di; Supplemental Figure S11A) and shared genomic intervals (Supplemental Figures S10B; S11B), with crisis sample genes also reflecting metabolic divergence. Together, these observations suggest that eccDNA-associated gene content reflects cellular processes engaged during crisis, including changes in energetic demand (Turner et al. 2017).

Since eccDNA may be generated by homology and non-homology dependent DNA repair (Cohen et al. 2006; Gadgil et al. 2024; Kang et al. 2025), we investigated eccDNA junction sequences for mechanistic insights. A prominent transformation in junction attributes was evident (Figure 5Ei), with progressive increases in the proportions of both template-switch (opposite strand orientation) junctions and translocations, aligned with the expansion in translocations observed for the crisis compared with Untransformed samples (Figure 5C). Whilst template-switched eccDNA junctions almost exclusively presented sequence microhomologies (Tatman and Black 2022) (Figure 5Eii), simple (same orientation) events were represented by blunt junctions as well as those bearing insertions or microhomologies. These observations may signify a prevalence of replicative or synthesis-dependent recombination processes underpinning template-switched events over larger genomic distances in contrast to non-homologous end-joining (NHEJ) localised at simple junctions (Lee et al. 2007; Sotiriou et al. 2016; Zhu et al. 2017; Kishkevich et al.

2022; Yang et al. 2023; Hu et al. 2024; Qin et al. 2025). Thus eccDNA provide a molecular readout of the deranged crisis genome.

Intersections of eccDNA genomic origins with sequence features (Figure 5F; Supplemental Figure S12) clearly distinguished events amplified from Untransformed MRC5 cells. In particular, the genomic intervals exclusive to Untransformed eccDNA ('U only') commanded greater association with centromeric (Figure 5Fi) and satellite, simple and LINE DNA repeats (Figure 5Fii; Supplemental Figure S12A) and fewer intersections with expressed genes and SINE repeats. Conversely, crisis-derived eccDNA more commonly originated in coding sequence (including fragile sites) and SINE DNA repeats; an attribute shared with telomere fusions (Supplemental Figure S12A). Associations with DNA repeats proved an effective means of sample stratification (Supplemental Figure S12B), effectively separating crisis from Untransformed samples, with comparable variance contributions from each DNA repeat class.

Overall, these discoveries support divergent mechanisms for synthesis of eccDNA in Untransformed (normal) and transformed (crisis) cells. Untransformed cells exhibit low levels of small eccDNA derived from long genes and repeat tracks, likely reflecting end-joining-mediated circularisation of replication byproducts. Crisis marks an upsurge in eccDNA formation, conceivably mediated by both replicative and homology-independent DNA repair processes, and more often occurring within actively transcribed chromatin.

eccDNA signatures of cellular stress and malignancy

To assess the relevance of our observations in the MRC5^{E6E7} crisis model to human disease, we investigated the impact of environmental stress (Supplemental Figure S13) and established malignancy (glioma; Supplemental Figure S14) for eccDNA profiles. Hypoxia influences both transcription (Johnson et al. 2008) and replication stress (Kindrick and Mole 2020; Ma et al. 2023) , so we first explored the effects of transient (24 hr) exposure to low (2%) compared with standard tissue culture (20%) oxygen (O_2) levels on eccDNA production and telomere fusions in MRC5 cells. Low O_2 resulted in higher eccDNA yields in the Untransformed cells (Supplemental Figure S13Ai), homogenising these to Early crisis levels. Accordingly, we determined a substantial (33%) enlargement in mean eccDNA size under low O_2 conditions (Supplemental Figure S13Aii), implicating cellular stress in the generation or maintenance of larger eccDNA. We also measured an increased incidence of simple eccDNA junctions (Supplemental Figure S13Aiii) closer to the chromosome ends (Supplemental Figure S13Aiv) and with enhanced associations with genes (Supplemental Figure S13Bi), simple and low-complexity repeats (Supplemental Figure S13Bii) relative to standard O_2 conditions. The

limited sizes of the datasets constrained our ability to detect direct overlaps between cognate fusion and eccDNA samples (Supplemental Figure S13Ci). Nonetheless, analysis at the gene level revealed shared amplifications across both SV types (Supplemental Figure S13Cii). We discerned 24 genes (1.53% of 1571 total) in common between fusion and eccDNA datasets, with overlaps between the Early crisis and low O_2-treated samples the most abundant. Examples of genes conjointly detected fused to telomeres and within eccDNA are displayed in Supplemental Figure S13D, where *VWF* and *CCSER1* appeared as fusions and eccDNA in Early crisis low O_2-treated samples, TTN was a fusion and eccDNA in standard O_2-treated samples and *EXT1* was identified in fusions from both Early crisis low and standard O_2-treated samples and an eccDNA in Untransformed standard O_2-treated samples. These results indicate a degree of parity amongst genes susceptible to DSB and recombination by quite different processes. However, the lack of junction proximity or similarity precludes definitive assignment of sequential or related mechanisms at present.

Gliomas, particularly glioblastoma multiforme (GBM), display considerable intra-tumoural heterogeneity and therapy resistance that may be conferred by eccDNA-driven oncogene expression (Noorani et al. 2022). We obtained unfixed tumour and matched-adjacent tissue from three patients with astrocytoma (WHO grade 2/3; *IDH1*, *ATRX* and *TP53* mutated) (Louis et al. 2021) and three patients with GBM (WHO grade 4; *TERT* promoter mutated; Supplemental Table S2). *ATRX* mutations are associated with decompressed chromatin at telomeres (Episkopou et al. 2014; Clynes et al. 2015) that is permissive of alternative lengthening of telomeres (ALT) and the production of extrachromosomal DNA containing telomere repeats (Lovejoy et al. 2012). We initially tested the capacity of eccDNA sequencing to detect such extrachromosomal telomere circles by evaluating the prevalence of telomere repeats (three contiguous hexamers) within SV (Supplemental Figure S14Ai). Notwithstanding inter-sample variability, eccDNA derived from astrocytoma patients exhibited a 4-fold higher incidence of telomere repeat modules than the GBM patient samples, despite having similar eccDNA content overall (Supplemental Figure S14Aii). We also detected examples of directly inverted telomere repeats in one astrocytoma patient sample that may indicate the circularisation of pre-existing telomere fusions (Muyas et al. 2024). Junction analyses revealed salient disease-specific characteristics (Supplemental Figure S14B), with evidence of enhanced microhomology (MH) usage in astrocytoma-derived eccDNA. Gene lengths were comparable across the samples (Supplemental Figure S14Ci), but located closer to the telomeres in eccDNA amplified from tumour compared with matched tissue samples (Supplemental Figure S14Cii), even though TL were not patently different (Supplemental Table S2).

Analysing underlying genomic features exposed a hypoxic signature for the astrocytoma tumour samples (Goncalves et al. 2025), comparable with the low O_2-treated MRC5 cells. The astrocytoma (but not GBM) tumour samples shared more overlapping genomic intervals with the totality of the MRC5 low (2%) O_2 samples than the standard (20%) O_2 samples (Supplemental Figure S14D). Repeat associations (Supplemental Fig. S14E) also mirrored those observed in low O_2 MRC5 samples, with increased intersections with simple, satellite and low-complexity repeats (Yehuda et al. 2025) and reduced overlap with LINE elements. STRING functional protein interaction analyses revealed a single reactome pathway enrichment in VEGFA-VEGFR2 signalling (FDR 0.0125; Supplemental Figure S14Fi) characteristic of chronic hypoxia (Shweiki et al. 1992; Blouw et al. 2003; Godard et al. 2003) for the GBM tumour sample. Circularised fragments of oncogenes (*CRK, SRC*, *ALK*), DNA repair components (*FANCC, FAN1, MGMT*; *FANCE, MLH1, PARP8, HIPK2*) and immune effectors (*HLA-E* and *C2*) were detected in GBM and astrocytoma (Supplemental Figure S14F) samples, with potential impact for pathological progression. We additionally detected amplification of the *EGFR* gene in one GBM patient (Supplemental Figure S14G) that was more extensive and exclusive than the recurrent punctate signal associated with simple repeats within the terminal intron. *EGFR* mutations and amplifications are key drivers of glioma (Libermann et al. 1985) and the same GBM patient was determined to have cytogenetic rearrangement of exons 14 and 15 of this gene (Supplemental Table S2). Thus, eccDNA profiles from patient samples capture key oncogenic processes driving malignancy.

Targeted evaluation of genome instability

Using a custom-designed targeted capture gene and genomics features panel, we pursued indices of genome-wide instability accompanying replicative crisis. We employed Manta (Chen et al. 2016) to call SV in pseudo tumour-normal sequential MRC5 sample pairs (Early vs. Untransformed; Deep vs. Early; Late vs. Deep). Filtering for 'breakend' (SV) calls outside of the targeted capture probe regions with junctions unique to individual samples revealed 38 translocations (Figure 6A) linking 54 genes from remote loci. SV were most abundant in Late crisis samples (Supplemental Figure S15A) and notably coincident with fragile sites (Supplemental Figure S15B), highlighting replication stress as a potential mechanism for the formation of these non-clonal rearrangements.

We next performed similar pairwise MRC5 sample evaluations of single nucleotide variants (SNV) for a more granular investigation of genome instability and mutational processes. Categorising the nucleotide substitutions (Figure 6B), we found that individual transitions were more common than any single transversion, but the overall proportion of

transversions was greater for all samples and elevated in the latest crisis samples (Supplemental Figure S15C). Recognising that transversions may have more deleterious consequences than transitions (Freudenberg-Hua et al. 2003; Liang et al. 2021), we explored SNV that altered with crisis transit. Among all SNV classes, only C>A transversions showed a notable increase with crisis progression (Figure 6B), as exemplified by the mutation observed within the first intron of *HAVCR2* (*TIM-3*; Supplemental Figure S16A). This SNV alters putative binding sites for regulators, including FOXQ1 (HFH1; Supplemental Figure S16B), that, concurrently with *HAVCR2*, is substantially upregulated in Late crisis MRC5^{E6E7} cells (Supplemental Figure S16C), affirming the possibility of functional consequences of such SNV during replicative crisis.

In accordance with the inclusion of peri/centromeric repeat targeted probes on the custom panel, we found that more than 60% all identified SNV were coincident with CenSat repeats (Figure 6C), although this proportion declined with crisis progression, consistent with the reductions in satellite and simple repeat associations (Figure 6D). A reciprocal rise in the proportions of SNV within coding sequence was most evident for the C>A transversions (Figure 6C) but overall incidence within promoter sequence was < 1% for any sample pairing, as anticipated from the panel design. These altered SNV distributions reflect a shift from replication slippage (Saayman et al. 2023; Maruta et al. 2024) or alignment ambiguity within satellite sequence (Altemose et al. 2022) towards a more compelling manifestation of the deteriorating integrity of the crisis genome revealed by our multiomics analyses (Figures 1-5). This was supported by evaluating the SNV classes within their trinucleotide context (Supplemental Figure S17), resulting in mutational signatures resembling 'ageing' profiles (Alexandrov et al. 2020; Degasperi et al. 2022).

Whilst inferring absolute copy number changes from targeted capture sequence data is problematic, we were able to evaluate relative copy number variation (CNV) using the same pseudo tumour-normal MRC5 sample pairings for sample normalisation implemented in VarScan 2 (Koboldt et al. 2012). We assessed the overlap of SNV and CNV with sites of single- and double-strand DNA breaks from our previous datasets (including ssDNA peaks, expressed genes, eccDNA, and telomere fusions; Figure 1 and (Liddiard et al. 2021)). These genomic features effectively distinguished SNV events from CNV gains and losses in samples progressing through replicative crisis ((Supplemental Figure S18A). CNV were less often coincident with R-loops and telomere fusions than SNV, but more frequently within genomic intervals shared with crisis-derived eccDNA, demonstrating a relationship between sporadic SV and more enduring gross copy number changes.

CN losses were more commonly associated with simple, satellite, SINE and rRNA repeats than CN gains (Figure 6E), conceivably explaining the reduced incidence of SNV within these sequences during crisis (Figure 6C, 6D) owing to real changes in genomic content. Pertinently, we also measured 1.38- and 1.2-fold reductions in the distance of CN losses (compared with gains) to telomere (Figure 6Fi) or centromere (Figure 6Fii) repeats on the same chromosome arm, respectively. This altered spatial distribution is consistent with satellite repeat rearrangements and repeat contractions reported during crisis (Stults et al., 2009; Liddiard et al., 2022), which are known to exacerbate replication stress (Gadgil et al. 2020; Shaikh et al. 2022; Ma et al. 2023) and erroneous repair (Hastings et al. 2009; Xu et al. 2017). Whilst extrapolation from the targeted capture methodology is limited, our data support the illustration of intrinsic instability at long genes and repeat tracts, with accumulating disruption of coding sequences as crisis advances.

Discussion:

Telomere-driven replicative crisis instigates global chromatin reorganisation

We previously demonstrated that inflammatory gene activation accompanies telomere fusion and genome instability in four independent human fibroblast models of replicative crisis (Liddiard et al. 2021). Here, using orthogonal sequencing approaches (Figure 1) in an MRC5 model, we have produced an integrated characterisation of replicative crisis (Supplemental Figure S18B), sampling earlier time points after HPV16 *E6E7* transduction and including Untransformed cell comparators to distinguish events driving entry into and progression through crisis.

Chromatin capture sequencing revealed replicative crisis to be a potent driver of expansive remodelling analogous to cellular differentiation rather than a more plastic stress response (Shanel et al. 2025). Telomere attrition reduces the density of proteins bound at the chromosome termini (Takai et al. 2010; Analikwu et al. 2025), establishing a more open chromatin configuration with crisis progression. Substantive chromatin reorganisation was exemplified by the elevated long-range (trans) interactions and contacts between eroded telomeres and centromere repeats (Figure 4A) in Deep crisis MRC5^{E6E7} cells. Telomere fusions mirrored this extended engagement (Figure 3A), with an increased prevalence of inter-chromosomal and concomitant reduction in local intra-chromosomal recombinations with crisis progression. Allelic resolution showed preferential engagement of the shorter ChrXpYp telomere with coding sequence and intra-chromosomal sites, whereas the longer telomere displayed increased associations with repeat

tracks (Figure 4F). This coalescence of the short telomere allele with expressed genes and the sister chromatid is consistent with our affirmation of this as the fusogenic allele in crisis (Liddiard et al. 2016) and the patent relationship between transcription, DSB and telomere fusions (Escudero et al. 2019; Liddiard et al. 2021).

Both TP53 (Scheffner et al. 1990) and RB1 (Dyson et al. 1989) function are abrogated in our MRC5^{E6E7} model of replicative crisis (Supplemental Figure S1), impacting chromatin structure (Gonzalo and Blasco 2005), as well as cell cycle progression and DNA repair (Obanya et al. 2025). Chromatin decompaction attenuates the insulating capacity of telomeres, derepressing gene expression (Baur et al. 2001) and condensin-mediated DNA loop extrusion, thereby constraining the error-free resolution of telomere fusions (Analikwu et al. 2025) that occur with increasing frequency in crisis (Supplemental Figure S1B). We additionally observed elevated incidence of larger and more complex eccDNA (Figure 5) and non-clonal translocations (Figure 6) at later stages of replicative crisis. Thus, telomere attrition and chromatin remodelling support the formation of alternative chromatin loops with extended genomic reach that enable synapsis of distant loci.

The release and redistribution around the genome (Stock et al. 2022) of DNA binding factors formerly sequestered within the telomere structure (Maillet et al. 1996; Platt et al. 2013) amplifies the persistent DNA damage signalled by the eroded telomere (Cesare et al. 2013; Nassour et al. 2024) (Supplemental Figure S5). The release of chromatin fragments (including replication intermediates and eccDNA) into the cytosol (Zhang et al. 2021) and telomeric repeat-containing transcripts (TERRA) into exosomes compounds the inflammatory environment (Wang et al. 2015; Lex et al. 2020). Telomeric structural transformations further impact the transcriptome through relief from the repressive telomere position effect (TPE) (Baur et al. 2001; Rey-Millet et al. 2023) that regulates expression of critical mediators of ageing and inflammation (Dong et al. 2021; Liddiard et al. 2021) enriched at the chromosome termini. Whilst our results distinguish telomere fusions from chromosomal interactions (Figures 3, 4), loci represented in both datasets propose the DNA damage response as a potent reorganising force (Supplemental Figure S5A) (Wu et al. 2024a), with binding sites for stress response mediators including BCL6 and EGR3 being over-represented in recombined sequences (Supplemental Figure S9).

eccDNA profiling reveals signatures of cellular stress and disease

The relative abundance and ease of eccDNA purification from crisis cells and patient samples make these SV more attractive and robust indicators of genome instability than telomere fusions, particularly where input material is

scarce. Notably, eccDNA derived from transformed MRC5^{E6E7} cells were quantitatively and qualitatively distinct from those amplified from Untransformed MRC5 (Figure 5, Supplemental Figures S10-S13), corroborating their potential as surrogates of malignancy (Bruhm et al. 2025). Lower yields of smaller eccDNA were harvested from Untransformed than transformed cells (Figure 5) and these were typified by simple junctions originating from longer genes and repeat elements that included centromeres and other satellite sequences. These characteristics suggest a constitutive NHEJ-mediated circularisation (Zhu et al. 2017; Hu et al. 2024; Kang et al. 2025; Qin et al. 2025) of the byproducts of replication and transcription at challenging repeat tracks and late-replicating genes with limited impact for cellular function (Møller et al. 2018). In contrast, eccDNA amplified from crisis MRC5^{E6E7} captured shorter genes with greater proportions of template-switched junctions and long-range complex translocation events, compatible with our chromatin capture data and suggestive of replicative repair (Sotiriou et al. 2016; Kishkevich et al. 2022; Zhang et al. 2023). Furthermore, we detected increased association with transcribed genes and SINE repeats, linking this transition to transcriptional reprogramming induced by crisis (Liddiard et al. 2021).

Regarding eccDNA as tangible indices of genome instability, we determined a sensitivity of profiles to environmental (Supplemental Figure S13) and pathological stressors (Supplemental Figure S14). Under conditions of transient low (2%) O_2, eccDNA purified from Untransformed MRC5 approximated the yields and size distributions characteristic of crisis MRC5^{E6E7} eccDNA (Supplemental Figure S13A), independent from effects on cell viability or proliferation. Cellular responses to mild hypoxia (Hu et al. 2003; Johnson et al. 2008; Kindrick and Mole 2020; Wu et al. 2022) resulted in eccDNA enriched in simple junctions capturing genes closer to telomeres, potentially reflecting NHEJ activity within sequences transcribed from the reservoir of inflammatory and immune regulators close to the chromosome ends (Lex et al. 2020; Lopes et al. 2021). Testifying to the replication stress exacerbated by hypoxia, eccDNA from cells cultured in low O_2 conditions were enriched in simple, satellite and low-complexity repeat motifs that may challenge replication fork or transcriptional progression (Hammond et al. 2002; Chan et al. 2008; Yehuda et al. 2025), facilitating eccDNA biogenesis (Qin et al. 2025). Amongst our cohort of glioma patients (Supplemental Table S2), eccDNA properties distinguished astrocytoma from GBM pathology and tumour tissue from matched-adjacent samples (Supplemental Figure S14). *ATRX*-mutant astrocytomas produced eccDNA enriched for telomeric and replication-stalling repeats (Clynes et al. 2015; Nguyen et al. 2017), with extended microhomology at junctions, consistent with replication stress and end-joining repair (Wimberly et al. 2013; Ngo et al. 2021). Whereas the astrocytoma tumour samples displayed significant parallels with MRC5 low O_2 cultures (Supplemental Figure S14D)

(Goncalves et al. 2025), the GBM tumours evidenced functional gene networks characteristic of the hypoxic environment that drives this aggressive pathology (Supplemental Figure S14F) (Park and Lee 2022; Marallano et al. 2024). Thus, by analysing eccDNA contents and junction features, we have been able to surmise both active gene networks and sites of replication stress. In a clinical setting, eccDNA profiling could likewise identify critical cancer dependencies for novel targeting strategies and therapeutic monitoring (Li et al. 2023; Wang et al. 2025).

Inter-relationship of structural variants

We previously reported the assimilation of circular plasmid and mitochondrial DNA into telomere fusions (Liddiard et al. 2016), raising the possibility of eccDNA being captured by deprotected telomeres during crisis. Moreover, we have exposed the association between telomere fusions, eccDNA and sites of copy number variations (CNV; Supplemental Figure S18 and (Escudero et al. 2019; Liddiard et al. 2021)) symptomatic of DNA excision and extrachromosomal amplification (Von Hoff et al. 1992; Verhaak et al. 2019). Accordingly, we identified recurrent genes incorporated into telomere fusions and eccDNA amplified from parallel MRC5 cell cultures confirming that destabilised loci are substrates for both forms of SV (Supplemental Figure S13D). With clinical relevance, we identified eccDNA comprising inverted telomere repeats amplified from a patient with *ATRX*- mutated astrocytoma, consistent with the production of telomeric circles in this cancer (Cesare and Griffith 2004). The concurrent amplification and cytogenetic rearrangement of *EGFR* observed for one GBM patient (Supplemental Figure S14G) is also suggestive of successive or interdependent mutational processes. Although we did not identify shared junctions among distinct SV in parallel analyses, our findings sustain the possibility of a common origin for telomere fusions and eccDNA in malignancy.

Overall, our integrated analyses reveal the critical contributions of telomere and centromere repeats to chromatin reorganisation under conditions of replicative and environmental stress. We demonstrate the interdependence of telomere attrition, replication and transcription in collective translation of the cellular stress response into three-dimensional structural variation within the evolving cancer genome (Supplemental Figure S18B). Our data support a model of replicative crisis in which the inherent instability of long, late-replicating sequences is progressively compounded by increasingly complex long-range interactions that disrupt crisis-response genes, shaping both cancer genotype and phenotype. We additionally uncover the unrealised potential of eccDNA as biomarkers of pathological processes - even in the absence of clonal amplifications. These findings highlight novel diagnostic opportunities as well as providing mechanistic insights into genome instability in replicative crisis.

Methods

Cells and treatments

MRC5 cells were authenticated by Short Tandem Repeat (STR) profiling with American Type Culture Collection (ATCC) and routinely screened for the absence of mycoplasma. Cells were cultured in Eagle's minimum essential medium (EMEM) supplemented with 1× non-essential amino acids, 10% (v/v) FCS, 1×10^5 IU/l penicillin, 100 mg/l streptomycin and 2 mM glutamine and buffered with 0.2% $NaHCO_3$ solution.

The crisis MRC5 cells were generated in our previous publication (Liddiard et al. 2021) using amphitropic retroviral vectors containing HPV16 *E6* and *E7* oncogenes (*E6E7*) and a neomycin resistance cassette (*NEO*), as outlined in (Bond et al. 1999). Selection of transduced and expressing $MRC5^{E6E7}$ cells was by culture in the presence of Geneticin (G418) at 0.4 mg/mL. Cells were maintained at 70-85% confluency, with population doubling (PD) calculated at each passage following cell counts using an NC-3000 image cytometer (Chemometec). The PD indicated in this manuscript refer to population growth after the point of retroviral transduction since this constitutes a bottleneck event (Supplemental Figure S1A). Crisis staging ('Early', 'Deep' and 'Late') was assigned according to the appearance and accumulation of telomere fusions at multiple chromosome ends (Supplemental Figure S1B) following telomere attrition (Supplemental Figure S1C).

For most experiments, cells were cultured at 37°C in 20% O_2 and 5% CO_2. For experiments comparing standard with low O_2 stimuli, parallel cell cultures of 7×10^5 Untransformed MRC5 or Early (PD23) crisis $MRC5^{E6E7}$ were established in incubators with 20% or 2% O_2, respectively, with nitrogen gas compensation and regular monitoring with a handheld gas analyser (Geotech G100).

Cell cycle analyses were performed using the Chemometec fixed cell cycle DAPI assay and analysed using Floreada.io software.

Chromatin capture (Capture-C)

Capture-C chromatin capture experiments were performed for $MRC5^{E6E7}$ Early (PD23) and Deep (PD47) crisis cells according to (Downes et al. 2022, 2023). *Nla*III restriction enzyme (NEB R0125) cleaved nuclear 3C libraries were prepared from each of 3 replicas of independent cell cultures of $MRC5^{E6E7}$ cells for each time point (5×10^6 cells each). Evaluation of library quality was made by agarose gel electrophoresis and qPCR. Libraries were sheared to 200

bp using an ME220 Covaris focused ultrasonicator and indexed using NEBNext® Multiplex Oligos for Illumina® (Primer Sets 1-3; E7335S, E7500S and E7710S) in a modification of the NEBNext® Ultra™ II DNA Library Prep Kit for Illumina® protocol. Each library was subjected to two rounds of capture hybridisation with each HPLC-purified 5′ biotinylated viewpoint probe set (Merck; Supplemental Methods Table S1) and amplification ahead of 150 bp paired-end sequencing on an Illumina MiSeq. The stringent design of viewpoint probes to capture interactions from the Chr17p and ChrXpYp (abridged to ChrXp throughout) subtelomeres was facilitated by the Capsequm tool (Davies et al. 2016). A non-telomeric control probe (XpG) was also designed within a non-coding locus 724 kb 5′ of the ChrXp subtelomere (XpT) probe for comparison with the subtelomere sequence context (Figure 2F; Supplemental Figure S2). Agilent Tapestation analyses were performed at multiple stages to verify library yields and size profiles.

Initial data analysis steps employed the Capcruncher software pipeline (Downes et al. 2022) to call genomic loci captured by each probe and produce BAM files for visualisation using the Integrative Genomics Viewer (IGV) (Robinson et al. 2011). For evaluations of long-range inter-chromosomal interactions, IGV was used to delineate and exclude local cis-interactions from downstream analyses. A signal threshold of 500 was applied to filter the remaining capture sites to mitigate the contribution of non-specific interactions to the analyses. Corroboration of the credibility of these trans interactions was provided by intersections with orthogonal datasets, including telomere fusion sequencing and extrachromosomal circular (eccDNA) sequencing. BLAT was used to verify selected alignments (Kent 2002). Allelic segregation of the ChrXp data was achieved by partitioning subtelomere alignments according to definitive presence of single nucleotide polymorphisms diagnostic of the long (A) or short (B) allele (Baird et al. 1995).

KAS-seq single-stranded DNA (ssDNA) mapping

KAS-seq identification of ssDNA genomic locations was implemented according to (Lyu et al. 2022). Three Early (PD23) and Deep (PD47) crisis MRC5^{E6E7} samples were labelled with N_3-kethoxal, sheared to 200 bp with the Covaris ME220 ultrasonicator and enriched following biotinylation using the AccuraDX KAS-Direct ssDNA Labeling and Enrichment Kit. Sequencing libraries were prepared from enriched and non-enriched fractions of the same samples (used as input controls) using the xGen™ ssDNA Low-Input DNA library prep (IDT 10009859) and xGen™ UDI Primers (IDT 10005975). Sequencing employed the Illumina NextSeq 550 high output 75 bp single-end sequencing platform

to meet the protocol requirements of 30 million reads per library. Ultimately, one crisis sample resulted in a low signal sequencing output and was eliminated from the downstream analyses.

Preliminary read processing and alignment was executed with KAS-Analyzer (V1.0) (Lyu et al. 2023) and ssDNA signal peaks in the enriched Early and Deep crisis samples compared with the input controls were identified using epic2 (Stovner and Sætrom 2019). DiffBind (Stark and Brown 2011; Ross-Innes et al. 2012) was used to perform differential analysis of consensus peaks, distinguishing peaks unique and common to the Early and Deep crisis states. An evaluation of false discovery rates (FDR) and fold changes of the differences was also reported. Full commands and settings developed for this study are available at https://github.com/e-coral/crisis_analyses and in the Supplemental material.

Circle-Seq

Glioma tissue samples were obtained from adult patients following informed consent, under the approval of the Welsh Neuroscience Research Tissue Bank (reference 19/WA/0058). Individual identifying information is not included in this manuscript. The methodology established by Møller (Møller 2020) was used to purify, amplify and sequence extrachromosomal DNA circles (eccDNA) from Untransformed MRC5, MRC5^{E6E7} and glioma patient tissue samples (Supplemental Figure S3). Approximately 7.5 × 10^5 cells or 4mm glioma tissue biopsies were harvested and processed for circular DNA extraction using the Plasmid Mini AX DNA kit (A&A Biotechnology). Digestion with Proteinase K was for 48 hr at 50°C at 700 RPM, reduction of mitochondrial DNA (mtDNA) with *Mss*I (*Pme*I) was for 1 hr at 37°C and elimination of linear genomic DNA involved 5 sequential doses of 25 U/sample Plasmid-safe DNase (Biosearch Technologies) over 36 hr at 37°C. Purified eccDNA were amplified by rolling circle amplification (RCA) with φ29 polymerase (Qiagen REPLI-g mini kit) over 60 hr and visualised by SYBR gold staining of electrophoresed products. Amplified eccDNA were sheared to 300-500 bp by ultrasonication with the Covaris M220 for Illumina 150 bp paired-end sequencing. Libraries from 500 ng sheared eccDNA were prepared utilising the NEBNext® Ultra™ II DNA Library Prep Kit for Illumina® and indices supplied in the NEBNext® Multiplex Oligos for Illumina® (Primer Sets 1-3). Agilent Tapestation analyses were performed at multiple stages to verify yields and size profiles. Samples were multiplexed and sequenced on the Illumina MiSeq.

Parallel PacBio long-read sequencing experiments were also performed for Untransformed MRC5 and Early and Deep crisis MRC5^{E6E7} cells, as well as a single glioma tumour sample in pre- and post-RCA formats. To preserve long-read

integrity, eccDNA samples were debranched with T7 endonuclease I at 37°C for 1 hr, purified using Agencourt AMPure XP magnetic beads at a 1:1 ratio and visualised by SYBR gold staining of electrophoresed products. Multiplexed amplicon libraries were prepared using the SMRTbell® prep kit 3.0 (102-182-700) in conjunction with the SMRTbell® barcoded adapter plate 3.0 (102-009-200). Verification and sizing of amplicons was conducted using an Agilent Fragment Analyser system and Qubit™ 4 Fluorometer. 100ng each adapted amplicon was pooled for PacBio sequencing using the Sequel II sequencing kit 2.0 (102-194-400) and SMRT® Cell 8M single-use tray (102-281-700). Sequencing was over 30 hr, resulting in 15 Gb HiFi reads.

Targeted capture sequencing experiments

For a focused investigation of genomic instability during replicative crisis, a custom targeted capture panel was designed incorporating 68 genes recurrently identified in our structural variant datasets; 3 with full-length probe coverage and 64 with exon-only (coding and UTR with 50 bp flanks) coverage. The panel additionally contained probes for capturing potentially unstable repeat elements, including selected LINE, centromeric satellites, subtelomere sequences, tRNA and rRNA clusters, G-quadruplex binding motifs and an MSI locus (details available on request). The custom panel was synthesised and quality validated by Twist Bioscience.

The Twist Bioscience cfDNA library preparation kit was used to prepare sequencing libraries from 50 ng each of MRC5 Untransformed and MRC5^{E6e7} Early (PD23), Deep (PD47 and Late (PD57) crisis genomic DNA that had been sheared (Covaris) to a mean fragment size of 350 bp. Amplified libraries were subjected to a 16 hr hybridisation with the custom probe panel at 70° C in a thermocycler. Following targeted enrichment, multiplexed libraries were sequenced using Illumina NextSeq 550 High-Output 300 cycle (2 × 150 bp) flow cell and reagents to achieve approximately 1500 × coverage of the 8 Mb panel.

Software availability

New computer code developed in this research is available at GitHub (https://github.com/e-coral) and as Supplemental Code.

Data Access

All raw and curated sequencing data generated in this study have been submitted to the NCBI BioProject database (https://www.ncbi.nlm.nih.gov/bioproject/) under the accession number PRJNA1181623.

Disclosures

Competing interests

The authors have no competing interests to declare.

Acknowledgements

This research was funded by Cancer Research UK grant C17199/A29202.

Harsh Bhatt is supported by RCS England Research Fellowship (520619) and Brain Research UK PhD Studentship (100044).

Joanne Morgan, NGS Technical Manager, Division of Psychological Medicine and Clinical Neurosciences, Cardiff University School of Medicine (PacBio sequencing).

Hughes Group: Genome Biology, University of Oxford Medical Sciences Division (Capture-C experiment consultation and training).

Wales Gene Park, Wales Genomic Health Centre, Cardiff (Illumina sequencing).

Welsh Neuroscience Research Tissue Bank (glioma patient samples).

Some of the results in this study are based on data generated by the TCGA Research Network: https://www.cancer.gov/tcga

Author contributions

Kate Liddiard conceived, designed and executed the project, analysed the data and prepared the manuscript for publication. Emmon Coral and Kez Cleal provided bioinformatics expertise, mapped all the datasets to the T2T CHM13v2.0/hs1 human reference and devised new scripts for data comparisons. Harsh Bhatt was instrumental in obtaining the glioma patient samples and also conducted telomere length measurements for these samples. Duncan Baird secured the funding that allowed the project to proceed and provided critical evaluation of the manuscript.

References

Alexandrov LB, Kim J, Haradhvala NJ, Huang MN, Tian Ng AW, Wu Y, Boot A, Covington KR, Gordenin DA, Bergstrom EN, et al. 2020. The repertoire of mutational signatures in human cancer. *Nature* **578**: 94–101.

Alitalo K, Schwab M, Lin CC, Varmus HE, Bishop JM. 1983. Homogeneously staining chromosomal regions contain amplified copies of an abundantly expressed cellular oncogene (c-myc) in malignant neuroendocrine cells from a human colon carcinoma. *Proc Natl Acad Sci USA* **80**: 1707–1711.

Altemose N, Logsdon GA, Bzikadze AV, Sidhwani P, Langley SA, Caldas GV, Hoyt SJ, Uralsky L, Ryabov FD, Shew CJ, et al. 2022. Complete genomic and epigenetic maps of human centromeres. *Science* **376**: eabl4178.

Analikwu BT, Deshayes A, van der Torre J, Guérin TM, Katan AJ, Béneut C, Barth R, Phipps J, Scolari V, Veaute X, et al. 2025. Telomeres stall DNA loop extrusion by condensin. *Cell Rep* **44**: 115900.

Arlt MF, Mulle JG, Schaibley VM, Ragland RL, Durkin SG, Warren ST, Glover TW. 2009. Replication stress induces genome-wide copy number changes in human cells that resemble polymorphic and pathogenic variants. *Am J Hum Genet* **84**: 339–350.

Arnould C, Rocher V, Saur F, Bader AS, Muzzopappa F, Collins S, Lesage E, Le Bozec B, Puget N, Clouaire T, et al. 2023. Chromatin compartmentalization regulates the response to DNA damage. *Nature* **623**: 183–192.

Bailey TL. 2021. STREME: accurate and versatile sequence motif discovery. *Bioinformatics* **37**: 2834–2840.

Baird DM, Jeffreys AJ, Royle NJ. 1995. Mechanisms underlying telomere repeat turnover, revealed by hypervariable variant repeat distribution patterns in the human Xp/Yp telomere. *EMBO J* **14**: 5433–5443.

Baird DM, Rowson J, Wynford-Thomas D, Kipling D. 2003. Extensive allelic variation and ultrashort telomeres in senescent human cells. *Nat Genet* **33**: 203–207.

Baron VT, Pio R, Jia Z, Mercola D. 2015. Early Growth Response 3 regulates genes of inflammation and directly activates IL6 and IL8 expression in prostate cancer. *Br J Cancer* **112**: 755–764.

Baur JA, Zou Y, Shay JW, Wright WE. 2001. Telomere position effect in human cells. *Science* **292**: 2075–2077.

Behrouzi R, Clipson A, Simpson KL, Blackhall F, Rothwell DG, Dive C, Mouliere F. 2025. Cell-free and extrachromosomal DNA profiling of small cell lung cancer. *Trends Mol Med* **31**: 64–78.

Berkemeier F, Cook PR, Boemo MA. 2025. DNA replication timing reveals genome-wide features of transcription and fragility. *Nat Commun* **16**: 4658.

Blouw B, Song H, Tihan T, Bosze J, Ferrara N, Gerber HP, Johnson RS, Bergers G. 2003. The hypoxic response of tumors is dependent on their microenvironment. *Cancer Cell* **4**: 133–146.

Böhly N, Schmidt A-K, Zhang X, Slusarenko BO, Hennecke M, Kschischo M, Bastians H. 2022. Increased replication origin firing links replication stress to whole chromosomal instability in human cancer. *Cell Rep* **41**: 111836.

Bond JA, Haughton MF, Rowson JM, Smith PJ, Gire V, Wynford-Thomas D, Wyllie FS. 1999. Control of replicative life span in human cells: barriers to clonal expansion intermediate between M1 senescence and M2 crisis. *Mol Cell Biol* **19**: 3103–3114.

Bruhm DC, Vulpescu NA, Foda ZH, Phallen J, Scharpf RB, Velculescu VE. 2025. Genomic and fragmentomic landscapes of cell-free DNA for early cancer detection. *Nat Rev Cancer* **25**: 341–358.

Capper R, Britt-Compton B, Tankimanova M, Rowson J, Letsolo B, Man S, Haughton M, Baird DM. 2007. The nature of telomere fusion and a definition of the critical telomere length in human cells. *Genes Dev* **21**: 2495–2508.

639 Cardenas MG, Oswald E, Yu W, Xue F, MacKerell AD, Melnick AM. 2017. The expanding role of the BCL6 oncoprotein
640 as a cancer therapeutic target. *Clin Cancer Res* **23**: 885–893.

641 Cer RZ, Bruce KH, Donohue DE, Temiz NA, Mudunuri US, Yi M, Volfovsky N, Bacolla A, Luke BT, Collins JR, et al. 2012.
642 Searching for non-B DNA-forming motifs using nBMST (non-B DNA motif search tool). *Curr Protoc Hum Genet*
643 **Chapter 18**: Unit 18.7.1-22.

644 Cesare AJ, Griffith JD. 2004. Telomeric DNA in ALT cells is characterized by free telomeric circles and heterogeneous
645 t-loops. *Mol Cell Biol* **24**: 9948–9957.

646 Cesare AJ, Hayashi MT, Crabbe L, Karlseder J. 2013. The telomere deprotection response is functionally distinct from
647 the genomic DNA damage response. *Mol Cell* **51**: 141–155.

648 Chan N, Koritzinsky M, Zhao H, Bindra R, Glazer PM, Powell S, Belmaaza A, Wouters B, Bristow RG. 2008. Chronic
649 hypoxia decreases synthesis of homologous recombination proteins to offset chemoresistance and
650 radioresistance. *Cancer Res* **68**: 605–614.

651 Chen X, Schulz-Trieglaff O, Shaw R, Barnes B, Schlesinger F, Källberg M, Cox AJ, Kruglyak S, Saunders CT. 2016.
652 Manta: rapid detection of structural variants and indels for germline and cancer sequencing applications.
653 *Bioinformatics* **32**: 1220–1222.

654 Chen Z, Qi Y, He J, Xu C, Ge Q, Zhuo W, Si J, Chen S. 2022. Distribution and characterization of extrachromosomal
655 circular DNA in colorectal cancer. *Mol Biomed* **3**: 38.

656 Cho NW, Dilley RL, Lampson MA, Greenberg RA. 2014. Interchromosomal homology searches drive directional ALT
657 telomere movement and synapsis. *Cell* **159**: 108–121.

658 Cleal K, Jones RE, Grimstead JW, Hendrickson EA, Baird DM. 2019. Chromothripsis during telomere crisis is
659 independent of NHEJ, and consistent with a replicative origin. *Genome Res* **29**: 737–749.

660 Clynes D, Jelinska C, Xella B, Ayyub H, Scott C, Mitson M, Taylor S, Higgs DR, Gibbons RJ. 2015. Suppression of the
661 alternative lengthening of telomere pathway by the chromatin remodelling factor ATRX. *Nat Commun* **6**: 7538.

662 Cohen Z, Bacharach E, Lavi S. 2006. Mouse major satellite DNA is prone to eccDNA formation via DNA Ligase IV-
663 dependent pathway. *Oncogene* **25**: 4515–4524.

664 Counter CM, Avilion AA, LeFeuvre CE, Stewart NG, Greider CW, Harley CB, Bacchetti S. 1992. Telomere shortening
665 associated with chromosome instability is arrested in immortal cells which express telomerase activity. *EMBO J* **11**:
666 1921–1929.

667 Davies JOJ, Telenius JM, McGowan SJ, Roberts NA, Taylor S, Higgs DR, Hughes JR. 2016. Multiplexed analysis of
668 chromosome conformation at vastly improved sensitivity. *Nat Methods* **13**: 74–80.

669 Degasperi A, Zou X, Amarante TD, Martinez-Martinez A, Koh GCC, Dias JML, Heskin L, Chmelova L, Rinaldi G, Wang
670 VYW, et al. 2022. Substitution mutational signatures in whole-genome-sequenced cancers in the UK population.
671 *Science* **376**.

672 Dekker J, Rippe K, Dekker M, Kleckner N. 2002. Capturing chromosome conformation. *Science* **295**: 1306–1311.

673 Dimitrova N, Chen Y-CM, Spector DL, de Lange T. 2008. 53BP1 promotes non-homologous end joining of telomeres
674 by increasing chromatin mobility. *Nature* **456**: 524–528.

675 Dixon JR, Selvaraj S, Yue F, Kim A, Li Y, Shen Y, Hu M, Liu JS, Ren B. 2012. Topological domains in mammalian
676 genomes identified by analysis of chromatin interactions. *Nature* **485**: 376–380.

677 Dong X, Sun S, Zhang L, Kim S, Tu Z, Montagna C, Maslov AY, Suh Y, Wang T, Campisi J, et al. 2021. Age-related
678 telomere attrition causes aberrant gene expression in sub-telomeric regions. *Aging Cell* **20**: e13357.

Downes DJ, Smith AL, Karpinska MA, Velychko T, Rue-Albrecht K, Sims D, Milne TA, Davies JOJ, Oudelaar AM, Hughes JR. 2023. Author Correction: Capture-C: a modular and flexible approach for high-resolution chromosome conformation capture. *Nat Protoc* **18**: 3155.

Downes DJ, Smith AL, Karpinska MA, Velychko T, Rue-Albrecht K, Sims D, Milne TA, Davies JOJ, Oudelaar AM, Hughes JR. 2022. Capture-C: a modular and flexible approach for high-resolution chromosome conformation capture. *Nat Protoc* **17**: 445–475.

Dubois F, Sidiropoulos N, Weischenfeldt J, Beroukhim R. 2022. Structural variations in cancer and the 3D genome. *Nat Rev Cancer* **22**: 533–546.

Dust K, Carpenter M, Chen JC-Y, Grant C, McCorrister S, Westmacott GR, Severini A. 2022. Human Papillomavirus 16 E6 and E7 Oncoproteins Alter the Abundance of Proteins Associated with DNA Damage Response, Immune Signaling and Epidermal Differentiation. *Viruses* **14**.

Dyson N, Howley PM, Münger K, Harlow E. 1989. The human papilloma virus-16 E7 oncoprotein is able to bind to the retinoblastoma gene product. *Science* **243**: 934–937.

Episkopou H, Draskovic I, Van Beneden A, Tilman G, Mattiussi M, Gobin M, Arnoult N, Londoño-Vallejo A, Decottignies A. 2014. Alternative Lengthening of Telomeres is characterized by reduced compaction of telomeric chromatin. *Nucleic Acids Res* **42**: 4391–4405.

Escudero L, Cleal K, Ashelford K, Fegan C, Pepper C, Liddiard K, Baird DM. 2019. Telomere fusions associate with coding sequence and copy number alterations in CLL. *Leukemia* **33**: 2093–2097.

Eugen-Olsen RAB, Hariprakash JM, Oestergaard VH, Regenberg B. 2025. Molecular mechanisms of extrachromosomal circular DNA formation. *Nucleic Acids Res* **53**.

Fong YW, Cattoglio C, Tjian R. 2013. The intertwined roles of transcription and repair proteins. *Mol Cell* **52**: 291–302.

Freudenberg-Hua Y, Freudenberg J, Kluck N, Cichon S, Propping P, Nöthen MM. 2003. Single nucleotide variation analysis in 65 candidate genes for CNS disorders in a representative sample of the European population. *Genome Res* **13**: 2271–2276.

Freudenreich CH, Su XA. 2016. Relocalization of DNA lesions to the nuclear pore complex. *FEMS Yeast Res* **16**.

Fritz AJ, Stojkovic B, Ding H, Xu J, Bhattacharya S, Gaile D, Berezney R. 2014. Wide-scale alterations in interchromosomal organization in breast cancer cells: defining a network of interacting chromosomes. *Hum Mol Genet* **23**: 5133–5146.

Gadgil RY, Rider SD, Shrestha R, Alhawach V, Hitch DC, Leffak M. 2024. Microsatellite break-induced replication generates highly mutagenized extrachromosomal circular DNAs. *NAR Cancer* **6**: zcae027.

Gadgil RY, Romer EJ, Goodman CC, Rider SD, Damewood FJ, Barthelemy JR, Shin-Ya K, Hanenberg H, Leffak M. 2020. Replication stress at microsatellites causes DNA double-strand breaks and break-induced replication. *J Biol Chem* **295**: 15378–15397.

Galaxy Community. 2024. The Galaxy platform for accessible, reproducible, and collaborative data analyses: 2024 update. *Nucleic Acids Res* **52**: W83–W94.

Geiller HEB, Harvey A, Jones RE, Grimstead JW, Cleal K, Hendrickson EA, Baird DM. 2022. ATRX modulates the escape from a telomere crisis. *PLoS Genet* **18**: e1010485.

Godard S, Getz G, Delorenzi M, Farmer P, Kobayashi H, Desbaillets I, Nozaki M, Diserens A-C, Hamou M-F, Dietrich P-Y, et al. 2003. Classification of human astrocytic gliomas on the basis of gene expression: a correlated group of genes with angiogenic activity emerges as a strong predictor of subtypes. *Cancer Res* **63**: 6613–6625.

719 Goncalves T, Cunniffe S, Ma TS, Mattis N, Rose AW, Kent T, Mole DR, Geiller HEB, van Bijsterveldt L, Humphrey TC, et
720 al. 2025. Elevated reactive oxygen species can drive the alternative lengthening of telomeres pathway in ATRX-null
721 cancers. *Nucleic Acids Res* **53**.

722 Gonzalo S, Blasco MA. 2005. Role of Rb family in the epigenetic definition of chromatin. *Cell Cycle* **4**: 752–755.

723 Gulen MF, Samson N, Keller A, Schwabenland M, Liu C, Glück S, Thacker VV, Favre L, Mangeat B, Kroese LJ, et al.
724 2023. cGAS-STING drives ageing-related inflammation and neurodegeneration. *Nature* **620**: 374–380.

725 Hammond EM, Denko NC, Dorie MJ, Abraham RT, Giaccia AJ. 2002. Hypoxia links ATR and p53 through replication
726 arrest. *Mol Cell Biol* **22**: 1834–1843.

727 Hastings PJ, Lupski JR, Rosenberg SM, Ira G. 2009. Mechanisms of change in gene copy number. *Nat Rev Genet* **10**:
728 551–564.

729 Hu C-J, Wang L-Y, Chodosh LA, Keith B, Simon MC. 2003. Differential roles of hypoxia-inducible factor 1alpha (HIF-
730 1alpha) and HIF-2alpha in hypoxic gene regulation. *Mol Cell Biol* **23**: 9361–9374.

731 Hu Q, Espejo Valle-Inclán J, Dahiya R, Guyer A, Mazzagatti A, Maurais EG, Engel JL, Lu H, Davis AJ, Cortés-Ciriano I, et
732 al. 2024. Non-homologous end joining shapes the genomic rearrangement landscape of chromothripsis from
733 mitotic errors. *Nat Commun* **15**: 5611.

734 Hung KL, Jones MG, Wong IT-L, Curtis EJ, Lange JT, He BJ, Luebeck J, Schmargon R, Scanu E, Brückner L, et al. 2024.
735 Coordinated inheritance of extrachromosomal DNAs in cancer cells. *Nature* **635**: 201–209.

736 Hung KL, Luebeck J, Dehkordi SR, Colón CI, Li R, Wong IT-L, Coruh C, Dharanipragada P, Lomeli SH, Weiser NE, et al.
737 2022. Targeted profiling of human extrachromosomal DNA by CRISPR-CATCH. *Nat Genet* **54**: 1746–1754.

738 Hung KL, Yost KE, Xie L, Shi Q, Helmsauer K, Luebeck J, Schöpflin R, Lange JT, Chamorro González R, Weiser NE, et al.
739 2021. ecDNA hubs drive cooperative intermolecular oncogene expression. *Nature* **600**: 731–736.

740 ICGC/TCGA Pan-Cancer Analysis of Whole Genomes Consortium. 2020. Pan-cancer analysis of whole genomes.
741 *Nature* **578**: 82–93.

742 Irastorza-Azcarate I, Kukalev A, Kempfer R, Thieme CJ, Mastrobuoni G, Markowski J, Loof G, Sparks TM, Brookes E,
743 Natarajan KN, et al. 2025. Extensive folding variability between homologous chromosomes in mammalian cells.
744 *Mol Syst Biol* **21**: 735–775.

745 Jaworski JJ, Pfuderer PL, Czyz P, Petris G, Boemo MA, Sale JE. 2025. ecDNA replication is disorganized and vulnerable
746 to replication stress. *Nucleic Acids Res* **53**.

747 Johnson AB, Denko N, Barton MC. 2008. Hypoxia induces a novel signature of chromatin modifications and global
748 repression of transcription. *Mutat Res* **640**: 174–179.

749 Kanda T, Otter M, Wahl GM. 2001. Mitotic segregation of viral and cellular acentric extrachromosomal molecules by
750 chromosome tethering. *J Cell Sci* **114**: 49–58.

751 Kang X, Li X, Zhou J, Zhang Y, Qiu L, Tian C, Deng Z, Liang X, Zhang Z, Du S, et al. 2025. Extrachromosomal DNA
752 replication and maintenance couple with DNA damage pathway in tumors. *Cell*.

753 Kent WJ. 2002. BLAT--the BLAST-like alignment tool. *Genome Res* **12**: 656–664.

754 Khadaroo B, Teixeira MT, Luciano P, Eckert-Boulet N, Germann SM, Simon MN, Gallina I, Abdallah P, Gilson E, Géli V,
755 et al. 2009. The DNA damage response at eroded telomeres and tethering to the nuclear pore complex. *Nat Cell*
756 *Biol* **11**: 980–987.

Khoury A, Achinger-Kawecka J, Bert SA, Smith GC, French HJ, Luu P-L, Peters TJ, Du Q, Parry AJ, Valdes-Mora F, et al. 2020. Constitutively bound CTCF sites maintain 3D chromatin architecture and long-range epigenetically regulated domains. *Nat Commun* **11**: 54.

Kim H, Nguyen N-P, Turner K, Wu S, Gujar AD, Luebeck J, Liu J, Deshpande V, Rajkumar U, Namburi S, et al. 2020. Extrachromosomal DNA is associated with oncogene amplification and poor outcome across multiple cancers. *Nat Genet* **52**: 891–897.

Kim NW, Piatyszek MA, Prowse KR, Harley CB, West MD, Ho PL, Coviello GM, Wright WE, Weinrich SL, Shay JW. 1994. Specific association of human telomerase activity with immortal cells and cancer. *Science* **266**: 2011–2015.

Kindrick JD, Mole DR. 2020. Hypoxic regulation of gene transcription and chromatin: cause and effect. *Int J Mol Sci* **21**.

Kishkevich A, Tamang S, Nguyen MO, Oehler J, Bulmaga E, Andreadis C, Morrow CA, Jalan M, Osman F, Whitby MC. 2022. Rad52's DNA annealing activity drives template switching associated with restarted DNA replication. *Nat Commun* **13**: 7293.

Koboldt DC, Zhang Q, Larson DE, Shen D, McLellan MD, Lin L, Miller CA, Mardis ER, Ding L, Wilson RK. 2012. VarScan 2: somatic mutation and copy number alteration discovery in cancer by exome sequencing. *Genome Res* **22**: 568–576.

Kraft K, Murphy SE, Jones MG, Shi Q, Bhargava-Shah A, Luong C, Hung KL, He BJ, Li R, Park SK, et al. 2025. Enhancer activation from transposable elements in extrachromosomal DNA. *Nat Cell Biol* **27**: 1914–1924.

Kumar P, Kiran S, Saha S, Su Z, Paulsen T, Chatrath A, Shibata Y, Shibata E, Dutta A. 2020. ATAC-seq identifies thousands of extrachromosomal circular DNA in cancer and cell lines. *Sci Adv* **6**: eaba2489.

Lai Z, Markovets A, Ahdesmaki M, Chapman B, Hofmann O, McEwen R, Johnson J, Dougherty B, Barrett JC, Dry JR. 2016. VarDict: a novel and versatile variant caller for next-generation sequencing in cancer research. *Nucleic Acids Res* **44**: e108.

Larizza L, Colombo EA. 2024. Interdependence between Nuclear Pore Gatekeepers and Genome Caretakers: Cues from Genome Instability Syndromes. *Int J Mol Sci* **25**.

Lee JA, Carvalho CMB, Lupski JR. 2007. A DNA replication mechanism for generating nonrecurrent rearrangements associated with genomic disorders. *Cell* **131**: 1235–1247.

Lemaître C, Grabarz A, Tsouroula K, Andronov L, Furst A, Pankotai T, Heyer V, Rogier M, Attwood KM, Kessler P, et al. 2014. Nuclear position dictates DNA repair pathway choice. *Genes Dev* **28**: 2450–2463.

Lex A, Gehlenborg N, Strobelt H, Vuillemot R, Pfister H. 2014. Upset: visualization of intersecting sets. *IEEE Trans Vis Comput Graph* **20**: 1983–1992.

Lex K, Maia Gil M, Lopes-Bastos B, Figueira M, Marzullo M, Giannetti K, Carvalho T, Ferreira MG. 2020. Telomere shortening produces an inflammatory environment that increases tumor incidence in zebrafish. *Proc Natl Acad Sci USA* **117**: 15066–15074.

Liang H, Xu Y, Chen M, Zhao J, Zhong W, Liu X, Gao X, Li S, Li J, Guo C, et al. 2021. Characterization of Somatic Mutations That Affect Neoantigens in Non-Small Cell Lung Cancer. *Front Immunol* **12**: 749461.

Libermann TA, Nusbaum HR, Razon N, Kris R, Lax I, Soreq H, Whittle N, Waterfield MD, Ullrich A, Schlessinger J. 1985. Amplification, enhanced expression and possible rearrangement of EGF receptor gene in primary human brain tumours of glial origin. *Nature* **313**: 144–147.

Liddiard K, Grimstead JW, Cleal K, Evans A, Baird DM. 2021. Tracking telomere fusions through crisis reveals conflict between DNA transcription and the DNA damage response. *NAR Cancer* **3**: zcaa044.

798 Liddiard K, Ruis B, Takasugi T, Harvey A, Ashelford KE, Hendrickson EA, Baird DM. 2016. Sister chromatid telomere
799 fusions, but not NHEJ-mediated inter-chromosomal telomere fusions, occur independently of DNA ligases 3 and 4.
800 *Genome Res* **26**: 588–600.

801 Lieberman-Aiden E, van Berkum NL, Williams L, Imakaev M, Ragoczy T, Telling A, Amit I, Lajoie BR, Sabo PJ,
802 Dorschner MO, et al. 2009. Comprehensive mapping of long-range interactions reveals folding principles of the
803 human genome. *Science* **326**: 289–293.

804 Lin C, Yang L, Tanasa B, Hutt K, Ju B, Ohgi K, Zhang J, Rose DW, Fu X-D, Glass CK, et al. 2009. Nuclear receptor-
805 induced chromosomal proximity and DNA breaks underlie specific translocations in cancer. *Cell* **139**: 1069–1083.

806 Lin TT, Letsolo BT, Jones RE, Rowson J, Pratt G, Hewamana S, Fegan C, Pepper C, Baird DM. 2010. Telomere
807 dysfunction and fusion during the progression of chronic lymphocytic leukemia: evidence for a telomere crisis.
808 *Blood* **116**: 1899–1907.

809 Li X, Manley JL. 2005. Inactivation of the SR protein splicing factor ASF/SF2 results in genomic instability. *Cell* **122**:
810 365–378.

811 Li Z, Wang B, Liang H, Li Y, Zhang Z, Han L. 2023. A three-stage eccDNA based molecular profiling significantly
812 improves the identification, prognosis assessment and recurrence prediction accuracy in patients with glioma.
813 *Cancer Lett* **574**: 216369.

814 Lopes I, Altab G, Raina P, de Magalhães JP. 2021. Gene size matters: an analysis of gene length in the human
815 genome. *Front Genet* **12**: 559998.

816 Lottersberger F, Karssemeijer RA, Dimitrova N, de Lange T. 2015. 53BP1 and the LINC Complex Promote Microtubule-
817 Dependent DSB Mobility and DNA Repair. *Cell* **163**: 880–893.

818 Louis DN, Perry A, Wesseling P, Brat DJ, Cree IA, Figarella-Branger D, Hawkins C, Ng HK, Pfister SM, Reifenberger G, et
819 al. 2021. The 2021 WHO Classification of Tumors of the Central Nervous System: a summary. *Neuro Oncol* **23**:
820 1231–1251.

821 Lovejoy CA, Li W, Reisenweber S, Thongthip S, Bruno J, de Lange T, De S, Petrini JHJ, Sung PA, Jasin M, et al. 2012.
822 Loss of ATRX, genome instability, and an altered DNA damage response are hallmarks of the alternative
823 lengthening of telomeres pathway. *PLoS Genet* **8**: e1002772.

824 Luo J, Li Y, Zhang T, Xv T, Chen C, Li M, Qiu Q, Song Y, Wan S. 2022. Extrachromosomal circular DNA in cancer drug
825 resistance and its potential clinical implications. *Front Oncol* **12**: 1092705.

826 Lyu R, Wu T, Park G, He Y-Y, Chen M, He C. 2023. KAS-Analyzer: a novel computational framework for exploring KAS-
827 seq data. *Bioinformatics Advances* **3**: vbad121.

828 Lyu R, Wu T, Zhu AC, West-Szymanski DC, Weng X, Chen M, He C. 2022. KAS-seq: genome-wide sequencing of single-
829 stranded DNA by N3-kethoxal-assisted labeling. *Nat Protoc* **17**: 402–420.

830 Ma TS, Worth KR, Maher C, Ng N, Beghè C, Gromak N, Rose AM, Hammond EM. 2023. Hypoxia-induced
831 transcriptional stress is mediated by ROS-induced R-loops. *Nucleic Acids Res* **51**: 11584–11599.

832 Maillet L, Boscheron C, Gotta M, Marcand S, Gilson E, Gasser SM. 1996. Evidence for silencing compartments within
833 the yeast nucleus: a role for telomere proximity and Sir protein concentration in silencer-mediated repression.
834 *Genes Dev* **10**: 1796–1811.

835 Makova KD, Weissensteiner MH. 2023. Noncanonical DNA structures are drivers of genome evolution. *Trends Genet*
836 **39**: 109–124.

837 Maliszewska-Olejniczak K, Bednarczyk P. 2024. Novel insights into the role of ion channels in cellular DNA damage
838 response. *Mutat Res Rev Mutat Res* **793**: 108488.

Marallano VJ, Ughetta ME, Tejero R, Nanda S, Ramalingam R, Stalbow L, Sattiraju A, Huang Y, Ramakrishnan A, Shen L, et al. 2024. Hypoxia drives shared and distinct transcriptomic changes in two invasive glioma stem cell lines. *Sci Rep* **14**: 7246.

Maruta G, Maeoka H, Tsunoda T, Akiyoshi K, Takagi S, Shirasawa S, Ishikura S. 2024. RAD52-mediated repair of DNA double-stranded breaks at inactive centromeres leads to subsequent apoptotic cell death. *Nucleic Acids Res* **52**: 12961–12975.

McClintock B. 1941. The stability of broken ends of chromosomes in zea mays. *Genetics* **26**: 234–282.

Miné-Hattab J, Rothstein R. 2012. Increased chromosome mobility facilitates homology search during recombination. *Nat Cell Biol* **14**: 510–517.

Mitsui Y, Schneider EL. 1976. Relationship between cell replication and volume in senescent human diploid fibroblasts. *Mech Ageing Dev* **5**: 45–56.

Møller HD, Bojsen RK, Tachibana C, Parsons L, Botstein D, Regenberg B. 2016. Genome-wide Purification of Extrachromosomal Circular DNA from Eukaryotic Cells. *J Vis Exp* e54239 |.

Møller HD, Mohiyuddin M, Prada-Luengo I, Sailani MR, Halling JF, Plomgaard P, Maretty L, Hansen AJ, Snyder MP, Pilegaard H, et al. 2018. Circular DNA elements of chromosomal origin are common in healthy human somatic tissue. *Nat Commun* **9**: 1069.

Møller HD. 2020. Circle-Seq: Isolation and Sequencing of Chromosome-Derived Circular DNA Elements in Cells. *Methods Mol Biol* **2119**: 165–181.

Mortenson KL, Dawes C, Wilson ER, Patchen NE, Johnson HE, Gertz J, Bailey SD, Liu Y, Varley KE, Zhang X. 2024. 3D genomic analysis reveals novel enhancer-hijacking caused by complex structural alterations that drive oncogene overexpression. *Nat Commun* **15**: 6130.

Muyas F, Rodriguez MJG, Cascão R, Afonso A, Sauer CM, Faria CC, Cortés-Ciriano I, Flores I. 2024. The ALT pathway generates telomere fusions that can be detected in the blood of cancer patients. *Nat Commun* **15**: 82.

Nassour J, Przetocka S, Karlseder J. 2024. Telomeres as hotspots for innate immunity and inflammation. *DNA Repair (Amst)* **133**: 103591.

Nassour J, Radford R, Correia A, Fusté JM, Schoell B, Jauch A, Shaw RJ, Karlseder J. 2019. Autophagic cell death restricts chromosomal instability during replicative crisis. *Nature* **565**: 659–663.

Neurohr GE, Terry RL, Lengefeld J, Bonney M, Brittingham GP, Moretto F, Miettinen TP, Vaites LP, Soares LM, Paulo JA, et al. 2019. Excessive cell growth causes cytoplasm dilution and contributes to senescence. *Cell* **176**: 1083-1097.e18.

Ngo GHP, Grimstead JW, Baird DM. 2021. UPF1 promotes the formation of R loops to stimulate DNA double-strand break repair. *Nat Commun* **12**: 3849.

Nguyen DT, Voon HPJ, Xella B, Scott C, Clynes D, Babbs C, Ayyub H, Kerry J, Sharpe JA, Sloane-Stanley JA, et al. 2017. The chromatin remodelling factor ATRX suppresses R-loops in transcribed telomeric repeats. *EMBO Rep* **18**: 914–928.

Noorani I, Mischel PS, Swanton C. 2022. Leveraging extrachromosomal DNA to fine-tune trials of targeted therapy for glioblastoma: opportunities and challenges. *Nat Rev Clin Oncol* **19**: 733–743.

Northcott PA, Lee C, Zichner T, Stütz AM, Erkek S, Kawauchi D, Shih DJH, Hovestadt V, Zapatka M, Sturm D, et al. 2014. Enhancer hijacking activates GFI1 family oncogenes in medulloblastoma. *Nature* **511**: 428–434.

Nurk S, Koren S, Rhie A, Rautiainen M, Bzikadze AV, Mikheenko A, Vollger MR, Altemose N, Uralsky L, Gershman A, et al. 2022. The complete sequence of a human genome. *Science* **376**: 44–53.

Obanya DI, Wootton LM, Morgan EL. 2025. Advances in understanding the mechanisms of the human papillomavirus oncoproteins. *Biochem Soc Trans* **53**: 565–577.

Ogbe A, Miao T, Symonds ALJ, Omodho B, Singh R, Bhullar P, Li S, Wang P. 2015. Early growth response genes 2 and 3 regulate the expression of bcl6 and differentiation of T follicular helper cells. *J Biol Chem* **290**: 20455–20465.

Oza P, Jaspersen SL, Miele A, Dekker J, Peterson CL. 2009. Mechanisms that regulate localization of a DNA double-strand break to the nuclear periphery. *Genes Dev* **23**: 912–927.

Park JH, Lee HK. 2022. Current understanding of hypoxia in glioblastoma multiforme and its response to immunotherapy. *Cancers (Basel)* **14**.

Peng L, Zhou N, Zhang C-Y, Li G-C, Yuan X-Q. 2022. eccDNAdb: a database of extrachromosomal circular DNA profiles in human cancers. *Oncogene* **41**: 2696–2705.

Penzo A, Dubarry M, Brocas C, Zheng M, Mangione RM, Rougemaille M, Goncalves C, Lautier O, Libri D, Simon M-N, et al. 2023. A R-loop sensing pathway mediates the relocation of transcribed genes to nuclear pore complexes. *Nat Commun* **14**: 5606.

Platt JM, Ryvkin P, Wanat JJ, Donahue G, Ricketts MD, Barrett SP, Waters HJ, Song S, Chavez A, Abdallah KO, et al. 2013. Rap1 relocalization contributes to the chromatin-mediated gene expression profile and pace of cell senescence. *Genes Dev* **27**: 1406–1420.

Qin L, Wu T, Zhen X, Zhao Y, Zhou J, Cheng S, Wang K, Qiao S, Huang D, Zhang H, et al. 2025. Extrachromosomal DNA biogenesis is dependent on DNA looping and religation by YY1-Lig3-PARylation complex. *Molecular cell*.

Qiu G-H, Zheng X, Fu M, Huang C, Yang X. 2021. The decreased exclusion of nuclear eccDNA: From molecular and subcellular levels to human aging and age-related diseases. *Ageing Res Rev* **67**: 101306.

Quinlan AR, Hall IM. 2010. BEDTools: a flexible suite of utilities for comparing genomic features. *Bioinformatics* **26**: 841–842.

Rey-Millet M, Pousse M, Soithong C, Ye J, Mendez-Bermudez A, Gilson E. 2023. Senescence-associated transcriptional derepression in subtelomeres is determined in a chromosome-end-specific manner. *Aging Cell* **22**: e13804.

Robinson JT, Thorvaldsdóttir H, Winckler W, Guttman M, Lander ES, Getz G, Mesirov JP. 2011. Integrative genomics viewer. *Nat Biotechnol* **29**: 24–26.

Ross-Innes CS, Stark R, Teschendorff AE, Holmes KA, Ali HR, Dunning MJ, Brown GD, Gojis O, Ellis IO, Green AR, et al. 2012. Differential oestrogen receptor binding is associated with clinical outcome in breast cancer. *Nature* **481**: 389–393.

Ryan RJH, Drier Y, Whitton H, Cotton MJ, Kaur J, Issner R, Gillespie S, Epstein CB, Nardi V, Sohani AR, et al. 2015. Detection of Enhancer-Associated Rearrangements Reveals Mechanisms of Oncogene Dysregulation in B-cell Lymphoma. *Cancer Discov* **5**: 1058–1071.

Saayman X, Graham E, Nathan WJ, Nussenzweig A, Esashi F. 2023. Centromeres as universal hotspots of DNA breakage, driving RAD51-mediated recombination during quiescence. *Mol Cell* **83**: 523-538.e7.

Sachs RK, Chen AM, Brenner DJ. 1997. Review: proximity effects in the production of chromosome aberrations by ionizing radiation. *Int J Radiat Biol* **71**: 1–19.

Sauter G, Maeda T, Waldman FM, Davis RL, Feuerstein BG. 1996. Patterns of epidermal growth factor receptor amplification in malignant gliomas. *Am J Pathol* **148**: 1047–1053.

Sawant DV, Sehra S, Nguyen ET, Jadhav R, Englert K, Shinnakasu R, Hangoc G, Broxmeyer HE, Nakayama T, Perumal NB, et al. 2012. Bcl6 controls the Th2 inflammatory activity of regulatory T cells by repressing Gata3 function. *J Immunol* **189**: 4759–4769.

Saxena S, Zou L. 2022. Hallmarks of DNA replication stress. *Mol Cell* **82**: 2298–2314.

Scheffner M, Werness BA, Huibregtse JM, Levine AJ, Howley PM. 1990. The E6 oncoprotein encoded by human papillomavirus types 16 and 18 promotes the degradation of p53. *Cell* **63**: 1129–1136.

Schenkel L, Wang X, Le N, Burger M, Kroschewski R. 2023. A dedicated cytoplasmic container collects extrachromosomal DNA away from the mammalian nucleus. *Mol Biol Cell* **34**: ar105.

Schwab M, Alitalo K, Klempnauer KH, Varmus HE, Bishop JM, Gilbert F, Brodeur G, Goldstein M, Trent J. 1983. Amplified DNA with limited homology to myc cellular oncogene is shared by human neuroblastoma cell lines and a neuroblastoma tumour. *Nature* **305**: 245–248.

Shaikh N, Mazzagatti A, De Angelis S, Johnson SC, Bakker B, Spierings DCJ, Wardenaar R, Maniati E, Wang J, Boemo MA, et al. 2022. Replication stress generates distinctive landscapes of DNA copy number alterations and chromosome scale losses. *Genome Biol* **23**: 223.

Shanel G, Hsieh T-HS, Cattoglio C, Haham HA, Chou H-J, Li JZ, Shamir R, Darzacq X, Elkon R. 2025. Transcriptional programs of cell identity and p53-induced stress responses are associated with distinctive features of spatial genome organization. *Nucleic Acids Res* **53**.

Shay JW, Pereira-Smith OM, Wright WE. 1991. A role for both RB and p53 in the regulation of human cellular senescence. *Exp Cell Res* **196**: 33–39.

Shimizu N, Misaka N, Utani K. 2007. Nonselective DNA damage induced by a replication inhibitor results in the selective elimination of extrachromosomal double minutes from human cancer cells. *Genes Chromosomes Cancer* **46**: 865–874.

Shweiki D, Itin A, Soffer D, Keshet E. 1992. Vascular endothelial growth factor induced by hypoxia may mediate hypoxia-initiated angiogenesis. *Nature* **359**: 843–845.

Simpson K, Jones RE, Grimstead JW, Hills R, Pepper C, Baird DM. 2015. Telomere fusion threshold identifies a poor prognostic subset of breast cancer patients. *Mol Oncol* **9**: 1186–1193.

Smit AFA, Hubley R, Green P. 2013. *RepeatMasker Open-4.0*. Institute for Systems Biology.

Sotiriou SK, Kamileri I, Lugli N, Evangelou K, Da-Ré C, Huber F, Padayachy L, Tardy S, Nicati NL, Barriot S, et al. 2016. Mammalian RAD52 Functions in Break-Induced Replication Repair of Collapsed DNA Replication Forks. *Mol Cell* **64**: 1127–1134.

Stark R, Brown G. 2011. DiffBind differential binding analysis of ChIP-Seq peak data. *In R package version* **100**.

Stock AJ, McDevitt RA, Puligilla C, Wang Y, Zhang Y, Wang K, Sun C, Becker KG, Lehrmann E, Wood WH, et al. 2022. Aberrant expression and localization of the RAP1 shelterin protein contribute to age-related phenotypes. *PLoS Genet* **18**: e1010506.

Stovner EB, Sætrom P. 2019. epic2 efficiently finds diffuse domains in ChIP-seq data. *Bioinformatics* **35**: 4392–4393.

Stoy H, Zwicky K, Kuster D, Lang KS, Krietsch J, Crossley MP, Schmid JA, Cimprich KA, Merrikh H, Lopes M. 2023. Direct visualization of transcription-replication conflicts reveals post-replicative DNA:RNA hybrids. *Nat Struct Mol Biol* **30**: 348–359.

Takai KK, Hooper S, Blackwood S, Gandhi R, de Lange T. 2010. In vivo stoichiometry of shelterin components. *J Biol Chem* **285**: 1457–1467.

Tatman PD, Black JC. 2022. Extrachromosomal Circular DNA from TCGA Tumors Is Generated from Common Genomic Loci, Is Characterized by Self-Homology and DNA Motifs near Circle Breakpoints. *Cancers (Basel)* **14**.

Trieu T, Martinez-Fundichely A, Khurana E. 2020. DeepMILO: a deep learning approach to predict the impact of non-coding sequence variants on 3D chromatin structure. *Genome Biol* **21**: 79.

Turner KM, Deshpande V, Beyter D, Koga T, Rusert J, Lee C, Li B, Arden K, Ren B, Nathanson DA, et al. 2017. Extrachromosomal oncogene amplification drives tumour evolution and genetic heterogeneity. *Nature* **543**: 122–125.

Verhaak RGW, Bafna V, Mischel PS. 2019. Extrachromosomal oncogene amplification in tumour pathogenesis and evolution. *Nat Rev Cancer* **19**: 283–288.

Vicario R, Peg V, Morancho B, Zacarias-Fluck M, Zhang J, Martínez-Barriocanal Á, Navarro Jiménez A, Aura C, Burgues O, Lluch A, et al. 2015. Patterns of HER2 Gene Amplification and Response to Anti-HER2 Therapies. *PLoS ONE* **10**: e0129876.

Vogt N, Gibaud A, Lemoine F, de la Grange P, Debatisse M, Malfoy B. 2014. Amplicon rearrangements during the extrachromosomal and intrachromosomal amplification process in a glioma. *Nucleic Acids Res* **42**: 13194–13205.

Von Hoff DD, McGill JR, Forseth BJ, Davidson KK, Bradley TP, Van Devanter DR, Wahl GM. 1992. Elimination of extrachromosomally amplified MYC genes from human tumor cells reduces their tumorigenicity. *Proc Natl Acad Sci USA* **89**: 8165–8169.

Wang J, Xu Z, Zhong Y, Yang J, Yang Z, Ye W, Wu Q, Du Y, Xing J, Xu M. 2025. Circulating extrachromosomal circular DNA in epithelial ovarian cancer reflects chemotherapeutic response and recurrence. *Exp Cell Res* **451**: 114695.

Wang Z, Deng Z, Dahmane N, Tsai K, Wang P, Williams DR, Kossenkov AV, Showe LC, Zhang R, Huang Q, et al. 2015. Telomeric repeat-containing RNA (TERRA) constitutes a nucleoprotein component of extracellular inflammatory exosomes. *Proc Natl Acad Sci USA* **112**: E6293-300.

Wei P-C, Chang AN, Kao J, Du Z, Meyers RM, Alt FW, Schwer B. 2016. Long neural genes harbor recurrent DNA break clusters in neural stem/progenitor cells. *Cell* **164**: 644–655.

Whalen JM, Dhingra N, Wei L, Zhao X, Freudenreich CH. 2020. Relocation of collapsed forks to the nuclear pore complex depends on sumoylation of DNA repair proteins and permits rad51 association. *Cell Rep* **31**: 107635.

Williamson LM, Lees-Miller SP. 2011. Estrogen receptor α-mediated transcription induces cell cycle-dependent DNA double-strand breaks. *Carcinogenesis* **32**: 279–285.

Wimberly H, Shee C, Thornton PC, Sivaramakrishnan P, Rosenberg SM, Hastings PJ. 2013. R-loops and nicks initiate DNA breakage and genome instability in non-growing Escherichia coli. *Nat Commun* **4**: 2115.

Wu Q, You L, Nepovimova E, Heger Z, Wu W, Kuca K, Adam V. 2022. Hypoxia-inducible factors: master regulators of hypoxic tumor immune escape. *J Hematol Oncol* **15**: 77.

Wu Z, Qu J, Liu G-H. 2024a. Roles of chromatin and genome instability in cellular senescence and their relevance to ageing and related diseases. *Nat Rev Mol Cell Biol* **25**: 979–1000.

Wu Z, Zhang W, Wang L, Leng J, Li Y, Fan Z, Zhan M, Cao L, Jiang Y, Jiang Y, et al. 2024b. Multi-omics integration reveals the oncogenic role of eccDNAs in diffuse large B-cell lymphoma through STING signalling. *Clin Transl Med* **14**: e1815.

Xu B, Li H, Perry JM, Singh VP, Unruh J, Yu Z, Zakari M, McDowell W, Li L, Gerton JL. 2017. Ribosomal DNA copy number loss and sequence variation in cancer. *PLoS Genet* **13**: e1006771.

Xu B, Sun Z, Liu Z, Guo H, Liu Q, Jiang H, Zou Y, Gong Y, Tischfield JA, Shao C. 2011. Replication stress induces micronuclei comprising of aggregated DNA double-strand breaks. *PLoS ONE* **6**: e18618.

Yang F, Su W, Chung OW, Tracy L, Wang L, Ramsden DA, Zhang ZZZ. 2023. Retrotransposons hijack alt-EJ for DNA replication and eccDNA biogenesis. *Nature* **620**: 218–225.

Yang L, Jia R, Ge T, Ge S, Zhuang A, Chai P, Fan X. 2022. Extrachromosomal circular DNA: biogenesis, structure, functions and diseases. *Signal Transduct Target Ther* **7**: 342.

Yan X, Mischel P, Chang H. 2024. Extrachromosomal DNA in cancer. *Nat Rev Cancer* **24**: 261–273.

Yehuda R, Dromi I, Levin Y, Carell T, Geacintov N, Livneh Z. 2025. Hypoxia-dependent recruitment of error-prone DNA polymerases to genome replication. *Oncogene* **44**: 42–49.

Yi E, Chamorro González R, Henssen AG, Verhaak RGW. 2022. Extrachromosomal DNA amplifications in cancer. *Nat Rev Genet* **23**: 760–771.

Yu Y, Ouyang Y, Yao W. 2018. shinyCircos: an R/Shiny application for interactive creation of Circos plot. *Bioinformatics* **34**: 1229–1231.

Zhang F, Khajavi M, Connolly AM, Towne CF, Batish SD, Lupski JR. 2009. The DNA replication FoSTeS/MMBIR mechanism can generate genomic, genic and exonic complex rearrangements in humans. *Nat Genet* **41**: 849–853.

Zhang T, Rawal Y, Jiang H, Kwon Y, Sung P, Greenberg RA. 2023. Break-induced replication orchestrates resection-dependent template switching. *Nature* **619**: 201–208.

Zhang X, Liu X, Du Z, Wei L, Fang H, Dong Q, Niu J, Li Y, Gao J, Zhang MQ, et al. 2021. The loss of heterochromatin is associated with multiscale three-dimensional genome reorganization and aberrant transcription during cellular senescence. *Genome Res* **31**: 1121–1135.

Zhou L, Tang W, Ye B, Zou L. 2024. Characterization, biogenesis model, and current bioinformatics of human extrachromosomal circular DNA. *Front Genet* **15**: 1385150.

Zhu J, Zhang F, Du M, Zhang P, Fu S, Wang L. 2017. Molecular characterization of cell-free eccDNAs in human plasma. *Sci Rep* **7**: 10968.

Figure legends

Figure 1: Multiomics profiling of telomere-driven replicative crisis in human fibroblasts

A A schematic of the human MRC5 fibroblast model of telomere-driven replicative crisis and the high-throughput sequencing (HTS) datasets analysed in this study. Untransformed and MRC5 transformed by retroviral transfer of human papillomavirus 16 (HPV) *E6* and *E7 (*E6E7) oncogenes (Bond et al. 1999) were sampled for targeted capture sequencing, Circle-Seq (Møller 2020), Fusion-seq (Liddiard et al. 2016), Kas-seq (Lyu et al. 2022) and chromatin capture (Downes et al. 2022) sequencing as indicated. Transformed MRC5 ($MRC5^{E6E7}$) were cultured through replicative crisis towards growth arrest with DNA extracted at Early (23 Population Doublings; PD23), Deep (PD47) and Late (PD57) time points after the appearance of telomere fusions. **Bi** The proportions of genomic intervals derived from key datasets analysed in this study that overlap with genomic features of interest; Genes, coding sequence; FRA, fragile sites; CenSat, centromere satellites; R-loops, 3-stranded nucleic acid structures. Samples include; a simulated dataset of 1 million random genomic loci (Random), telomere fusions sequenced from $MRC5^{E6E7}$ crisis cells (Fusions), single-strand DNA (ssDNA) peaks determined by KAS-seq in Early (E) or Deep (D) crisis samples, Chromatin capture (CC) datasets collected at Early (E) and Deep (D) time points using hybridisation probes targeting the Chr17p (17pT) and ChrXpYp (XpT) telomere-adjacent sequence, and extra-chromosomal circular DNA (eccDNA) from Untransformed (U) and $MRC5^{E6E7}$ cells at Early (E) and Deep (D) crisis stages. **ii** A Principle Component Analysis (PCA) plot (Galaxy Community 2024) of an extended range of datasets reveals the clustering of these samples based on the variance of these core parameters (indicated in the table below). Samples are encoded as in **Bi**, with the inclusion of ssDNA peaks common to both Early and Deep crisis samples (S; shared), CC datasets from Early (E) and Deep (D) crisis stages generated using the non-coding ChrXp genomic locus hybridisation probe (XpG), and eccDNA datasets exclusive to Untransformed MRC5 (UO) or crisis $MRC5^{E6E7}$ (E6E7) cells.

Figure 2: Correspondence of single-strand DNA peaks with transcription and telomere-interacting sites in replicative crisis

Ai UpSet plot (Lex et al. 2014) depicting the overlaps (intersections) between $MRC5^{E6E7}$ KAS-seq datasets (EARLY; DEEP, crisis stages; SHARED, ssDNA peaks common to both stages) and coding sequence (GENES) or genes expressed by $MRC5^{E6E7}$ during crisis (Liddiard et al. 2021) (EXPRESSED). Connected dots indicate the datasets included in each intersection, with vertical bars showing the number of elements in that intersection, enumerated above the bars. Key

intersections are boxed in red. The dataset (Set) sizes in nucleotide base pairs (bp) are depicted as horizontal bars. **ii** The proportions of genomic intervals associated with the specified Kas-seq ssDNA datasets (EARLY; DEEP, crisis stages; SHARED, common to both stages) or 1 million random genomic loci that intersect with genomic features are displayed. Genes, coding sequence; Expressed, genes expressed by MRC5^{E6E7} during crisis (Liddiard et al. 2021); R-loops, 3-stranded nucleic acid structures. Differences were evaluated using the N-1 Chi-square method (*P*-values indicated). **B** Pie charts representing the fractions of Early and Deep crisis genes with ssDNA enriched at 5′ or 3′ locations or detected at both 5′ and 3′ ends or throughout the entire gene body. Undetermined describes negligible ssDNA signal. The results of N-1 Chi-square comparisons of the 5′ and 3′ ssDNA gene enrichments are denoted next to the Deep crisis chart. **C** 5 kb genomic sequence extending from the 3′ termini of genes with prevailing 3′ ssDNA signal was assessed for presence of putative non-B DNA repeat motifs (X-axis; defined by Advanced Biomedical Computational Science (ABCS) (Cer et al. 2012)). Incidence rates (number of motifs per kilobase of input DNA) were compared for Early and Deep crisis samples and the *P*-value for the incidence rate ratio is indicated. G4; G-quadruplex repeats.

Figure 3: The changing profiles of telomere interactions and fusions during crisis transition

A The proportions of mapped telomere fusion sequences generated from Early (PD23) MRC5^{E6E7} crisis cells in this study that were classified as ‘Genomic’ (telomere fused to internal genomic locus), ‘Intra’ (intra-chromosomal; telomeres of the same chromosome fused together) or ‘Inter’ (inter-chromosomal; telomeres of different chromosome fused together) are presented alongside comparable data for PD45 and PD49 MRC5^{E6E7}crisis cells detailed in our former study (Liddiard et al. 2021). The black triangle and darker coloured bars indicate the progression of replicative crisis. Statistical analyses employed the N-1 Chi-square method. **B** Circos plots (Yu et al. 2018) depicting all MRC5^{E6E7} Early and Deep crisis chromatin interactions with **i** Chr17p (17pT) or **ii** ChrXp (XpT) telomere-adjacent probes (17pT) determined using Capture-C presented as concentric perimeter tracks. Track height indicates signal intensity. Fusions between the **i** Chr17p (red) or **ii** ChrXp (blue) telomeres and genomic sites span the circle centres. Peripheral black lines underneath the chromosome identities demarcate the centromere and pericentromeric (CenSat) repeats. **C** Cartoons depicting the sequence contexts and human T2T-CHM13/hs1 genomic reference (Nurk et al. 2022) coordinates of the Chr17p (17pT), ChrXp (XpT) and internal genomic control (XpG) probes used in the chromatin Capture-C experiments. L and R denote the positions of the dual oligonucleotide

076 probes at each location (detailed in Supplementary Methods Table 1). Adjacent DNA repeats are represented by
077 coloured blocks; LTR, long terminal repeat; LINE, long interspersed repeat; SINE, short interspersed repeat; DNA, DNA
078 repeat.

079 **Figure 4: Crisis represents a transition in chromatin state and long-range chromosomal interactions**

080 **Ai** Normalised read counts for all long-range trans compared with local cis chromatin Capture-C interactions
081 determined by the Capcruncher pipeline. Triplicate samples of the Early and Deep crisis MRC5^{E6E7} sampling points
082 using the Chr17p and ChrXp telomere-adjacent (17pT; XpT) and the ChrXp internal genomic (XpG) probes are
083 displayed as means with 95% confidence intervals (CI), analysed using paired parametric *t*-tests. The mean sample
084 percentages of interactions captured by the 17pT, XpT and XpG probes in Early and Deep crisis that **ii** overlap with
085 ALR/alpha satellite repeats **iii** are within 10 Mb of centromere or **iv** within 10 Mb of telomere sequences are
086 presented and compared using the N-1 Chi-square method. **B** The proportions of unique genes identified within crisis
087 MRC5^{E6E7} telomere fusions sequenced in this and our former study (Liddiard et al. 2021) that overlap with genes
088 captured by 17pT, XpT or XpG probes in chromatin Capture-C experiments is shown and evaluated using the N-1 Chi-
089 square method. **C** The proportions of genomic intervals associated with telomere fusion and chromatin Capture-C
090 datasets that intersect with genes expressed in comparable crisis stage MRC5^{E6E7} samples (Liddiard et al. 2021) were
091 computed using BEDTools intersect intervals (Quinlan and Hall 2010). Intersections with MRC5^{E6E7} telomere fusions
092 were compared with intersections of each individual 17pT, XpT or XpG probe Capture-C dataset (E, Early crisis; D,
093 Deep crisis) using the N-1 Chi-square method. **D** The proportions of genomic intervals derived from chromatin
094 Capture-C datasets (17pT, XpT and XpG probes; Early and Deep crisis stages) that intersect with DNA repeats defined
095 by RepeatMasker (Smit et al. 2013) (X-axis) are presented. The order of the datasets displayed corresponds to the
096 adjacent key. DNA, DNA repeat; LINE, long interspersed repeat; SINE, short interspersed repeat; LTR, long terminal
097 repeat. Evaluation of differences employed the N-1 Chi-square method. **E** XpT chromatin Capture-C interactions were
098 categorised according to the presence or absence of single nucleotide variants (SNV) characteristic of the long (A) or
099 short (B) ChrXp telomere allele (Baird et al. 2003). The percentages of 'All, 'Intra'- or 'Inter'-chromosomal XpT
100 interactions are compared for the Early and Deep crisis stages using the N-1 Chi-square method. **F** The proportions of
101 genomic intervals associated with ChrXp A or B total allelic contacts that intersect with **i** Genes, Expressed genes and
102 centromeric satellite (CenSat) repeats or **ii** SINE and satellite DNA repeats (delineated by RepeatMasker (Smit et al.

2013)) were analysed using the same methodology. **G** The lengths of all genes (log_{10} scaling; means annotated within boxes below the X-axis; bp, base pairs) captured by **i** the 17pT and XpT subtelomere probes at Early and Deep crisis stages and **ii** the XpT A or B alleles at both crisis stages. Means with 95% CI were compared using unpaired non-parametric Mann-Whitney U-tests.

Figure 5: Distinct quantities and characteristics of extra-chromosomal circular DNA are detected in untransformed and crisis MRC5 cells

A The quantities of all sequenced eccDNA junctions amplified from Untransformed MRC5 (U; 6 replicas) and Early (9 replicas) and Deep (6 replicas) crisis $MRC5^{E6E7}$ cells are displayed by chromosome. **B** Bar chart displaying mean sizes in bp with 95% CI for **i** Illumina short-read sequenced or **ii** PacBio long-read sequenced simple eccDNA. Mean values × 10^5 bp are displayed in coloured boxes below the bars. Statistical evaluation was by Mann-Whitney unpaired non-parametric U-tests. **C** Stacked chart displaying the relative proportions of distinct structural variants (SV) called from the PacBio long-read eccDNA sequencing data for Untransformed MRC5 and Early and Deep crisis $MRC5^{E6E7}$ cells; DEL, deletions; DUP, duplications; INS, insertions; INV, inversions; TRA, translocations; BND, breakend rearrangements that cannot unambiguously be categorised as single canonical SV. Vertical black lines connect datasets evaluated using the N-1 Chi-square method, with results displayed as: * P<0.05; ** P<0.01; *** P<0.001; **** P<0.0001. **Di** Venn diagram showing the numbers of direct gene overlaps amongst the eccDNA derived from Untransformed MRC5 and Early or Deep crisis $MRC5^{E6E7}$ cells. **ii** The lengths of genes (means annotated below the X-axis; bp, base pairs) uniquely-identified within genomic intervals assigned to eccDNA from Untransformed (U only) or transformed (E6E7 only) MRC5 cells are displayed in a bar chart with means and 95% CI. Mean values × 10^5 bp are displayed in coloured boxes below the bars. Differences were assessed by unpaired parametric *t*-tests with Welch's correction for unequal standard deviations (SD). **Ei** The proportions eccDNA junctions amplified from Untransformed, Early and Deep crisis MRC5 samples that comprise DNA segments derived from the same strand ('Simple') or opposing strands ('Template-switch') or distant chromosome locations ('Translocation') are depicted as a bar chart of means with 95% CI and compared using parametric unpaired *t*-tests with Welch's correction. A schematic depicting DNA orientation at the eccDNA junctions (chrA, chrB) is shown below the chart. **ii** Simple and template-switch junctions sequenced from all samples were examined for microhomology usage > 1 bp (MH; pale grey) and inserted DNA sequences > 1 bp (INS; black) or blunt joins (BLUNT; white). The proportions of junctions displaying each feature

are presented in a bar chart and evaluated using unpaired non-parametric Mann-Whitney U-tests. **Fi** Genomic intervals for eccDNA derived from Untransformed MRC5, Early and Deep crisis MRC5^{E6E7} or subsamples comprising Untransformed-only (U only) or transformed-only (E6E7 only) were intersected with the features indicated on the X-axis; Genes, all coding sequence; Expressed, genes expressed in crisis MRC5^{E6E7}; FRA, fragile sites; CenSat, peri/centromeric repeats; R-loops, trinucleotide DNA structures. Pairwise comparisons were performed using the N-1 Chi-square method and results are displayed as: * P<0.05; ** P<0.01; *** P<0.001; **** P<0.0001. **ii** The same eccDNA sample (indicated on the X-axis) genomic intervals were intersected with DNA repeats (defined by RepeatMasker (Smit et al. 2013)) and the proportions of each repeat class (right-hand colour key) are displayed in a stacked bar chart. The notable differences between the discrete Untransformed-only (U only) and transformed-only (E6E7 only) were evaluated with the N-1 Chi-square method, as in **i**. RC, Rolling Circle repeats; RNA, grouped representation of all classes of RNA repeats (rRNA, tRNA, snRNA, scRNA and srpRNA).

Figure 6: Mutational shifts with crisis progression

A The genomic distributions of 38 structural variants (SV) called by Manta (Chen et al. 2016) from targeted capture sequence data for Untransformed (U; pale grey) and MRC5^{E6E7} undergoing replicative crisis (E, D, L; Early, Deep and Late crisis; mid-grey to black) depicted as Circos plot (Yu et al. 2018) links. Genes incorporated into the SV are numbered and decoded in Supplemental Table S3. The chromosome identities, centromere positions (denoted by CenSat repeats) and locations of the genome instability probes featured on the targeted capture panel are indicated. **B** The percentages of all single nucleotide variants (SNV) called using VarDict (Lai et al. 2016) for pairwise pseudo tumour-normal (Early crisis vs Untransformed, Deep vs Early crisis and Late vs Deep crisis) comparisons of MRC5 samples sequenced following targeted capture are displayed. Transitions (purine-purine or pyrimidine-pyrimidine) underscored in orange (left) and transversions (purine ↔ pyrimidine) in green (right). Comparisons of SNV proportions in progressive samples were performed with the N-1 Chi-square method and results are displayed as: * P<0.05; ** P<0.01; *** P<0.001; **** P<0.0001. **C** The proportions of all SNV or specifically C>T transitions or C>A transversions identified in pairwise pseudo tumour-normal MRC5 comparisons that coincide with coding sequence (Genes) or centromeric satellites (CenSat) are displayed in a bar chart and compared using the N-1 Chi-square method. **D** Overlaps between all SNV called from progressive pseudo tumour-normal MRC5 sample pairings and specific repeat elements (X-axis) are displayed as proportions of the total overlaps with repeats and evaluated in the

same way (P-values recorded); SINE, short interspersed repeat; LINE, long interspersed repeat. **Ei** A parallel plot displaying the proportions of specific DNA repeat elements (listed along the top) comprising the total repeats intersections with the altered copy number (CN) datasets indicated on the right (lower Gains and upper Losses for each pairwise sample comparison). 'ALL' represents the genomic intervals common to all pairwise CN Gains or CN Losses. The upper and lower boundaries of the proportions are annotated at the top and bottom of the chart, respectively; LTR, long terminal repeat; rRNA, ribosomal RNA repeats. **ii** A bar chart displaying the most salient differentials (evaluated using the N-1 Chi-square method) between the genomic intervals common to CN Gains or CN Losses with respect to DNA repeat associations. **F** The distance to the **i** telomere on the same chromosome arm or **ii** centromere of CN Gains and Losses common to all pairwise sample comparisons; statistical assessments by Mann-Whitney unpaired non-parametric U-tests.

Figure1

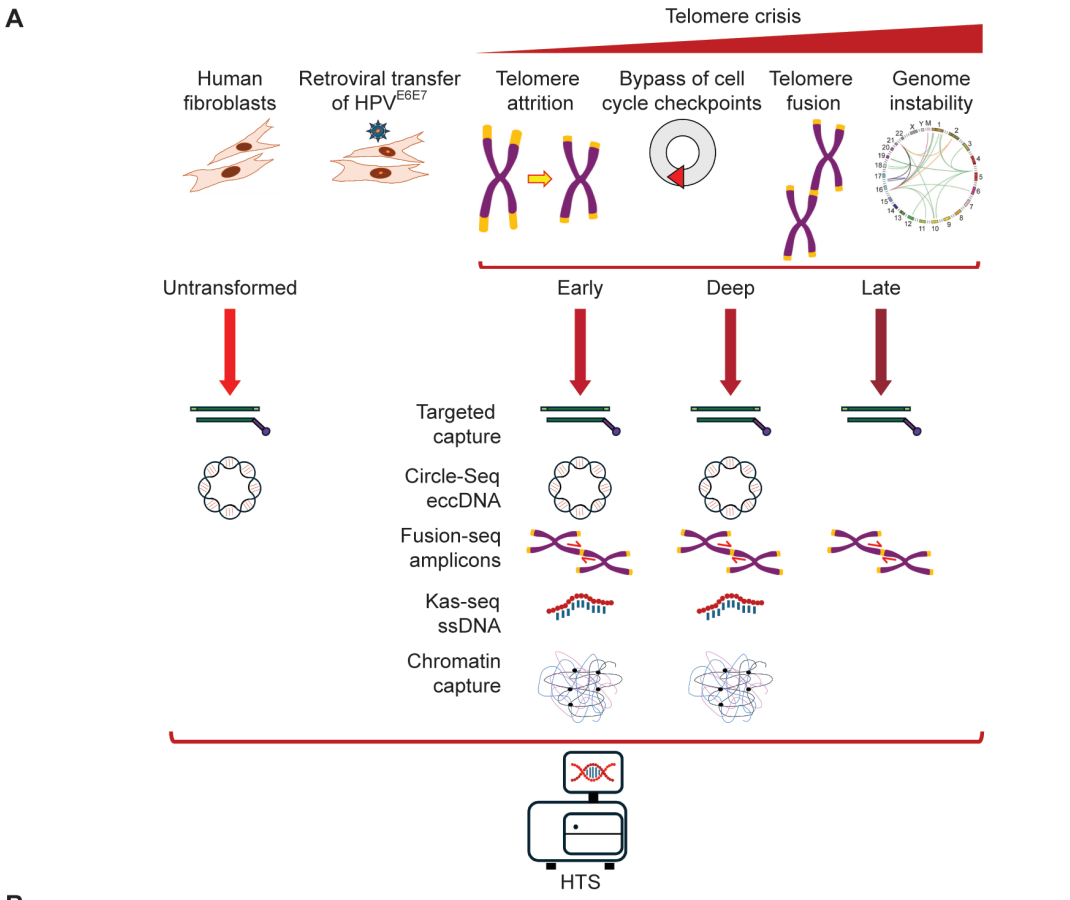

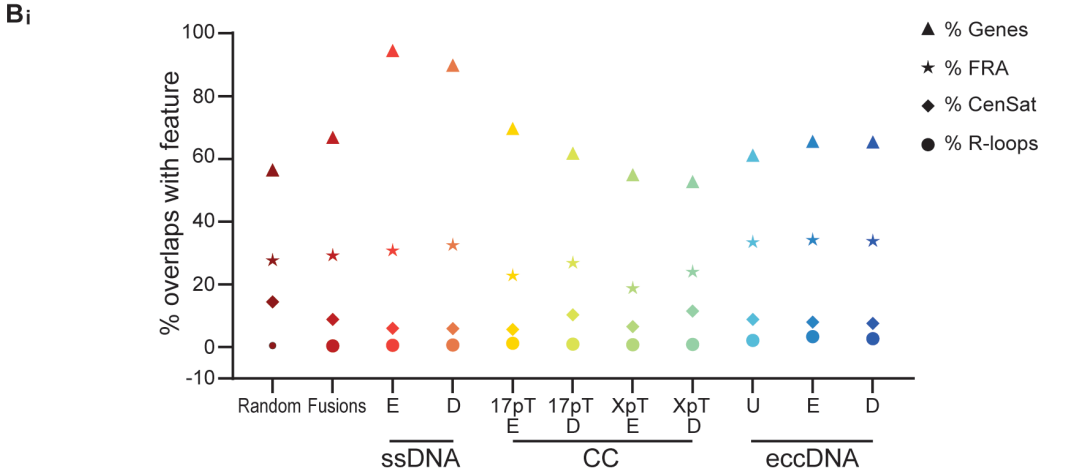

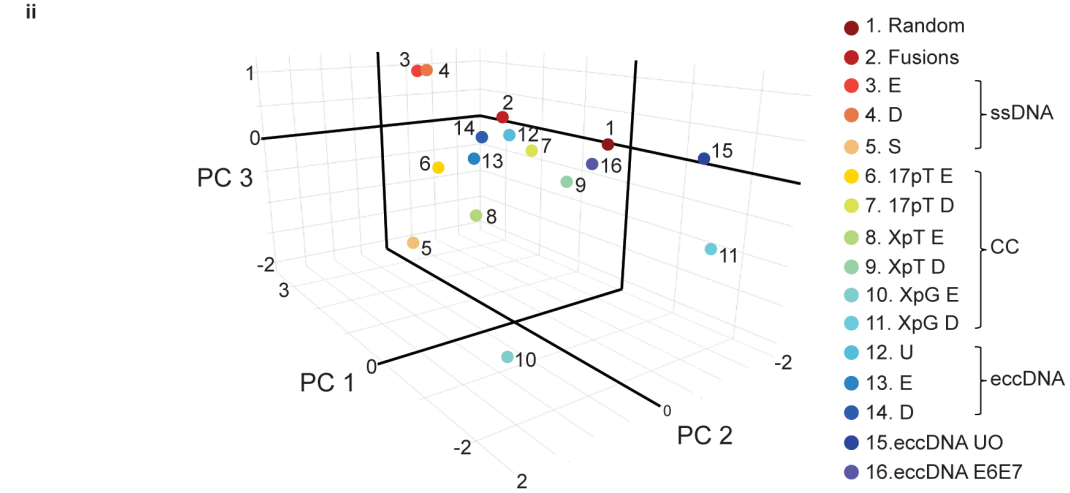

Parameter	PC1 (57.4%)	PC2 (22.5%)	PC3 (15.3%)
% Genes	0.605	0.029	-0.296
% FRA	0.529	-0.454	-0.417
% CenSat	-0.358	-0.871	0.022
% R-loops	0.475	-0.188	0.859

Figure 2

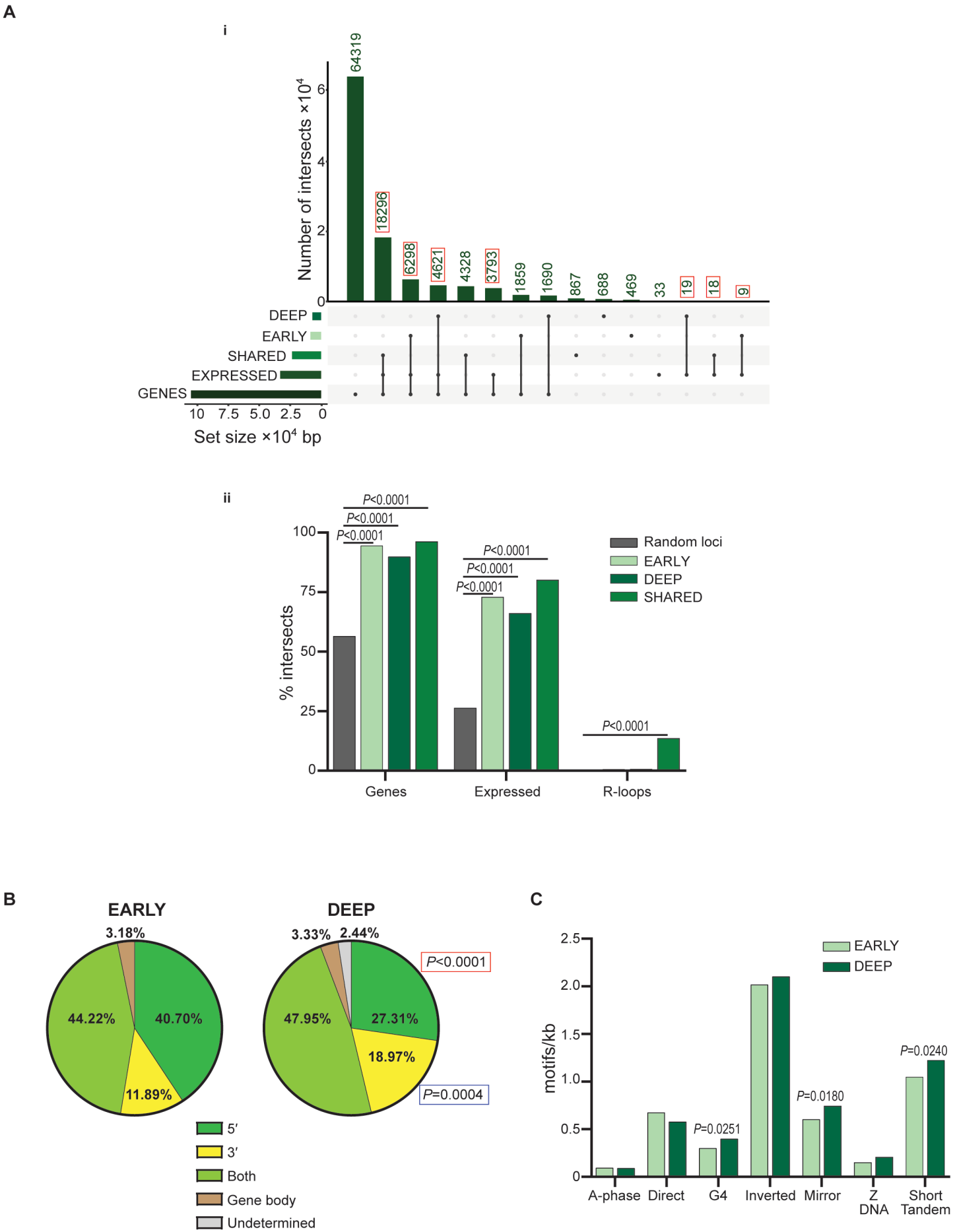
A
i
Number of intersects ×10^4
64319
18296
6298
4621
4328
3793
1859
1690
867
688
469
33
19
18
9
DEEP
EARLY
SHARED
EXPRESSED
GENES
10 7.5 5.0 2.5 0
Set size ×10^4 bp
ii
% intersects
P<0.0001
Random loci
EARLY
DEEP
SHARED
Genes
Expressed
R-loops
B
EARLY
DEEP
3.18%
44.22%
40.70%
11.89%
3.33%
2.44%
47.95%
27.31%
18.97%
P<0.0001
P=0.0004
5′
3′
Both
Gene body
Undetermined
C
motifs/kb
EARLY
DEEP
P=0.0251
P=0.0180
P=0.0240
A-phase
Direct
G4
Inverted
Mirror
Z DNA
Short Tandem

Figure 3

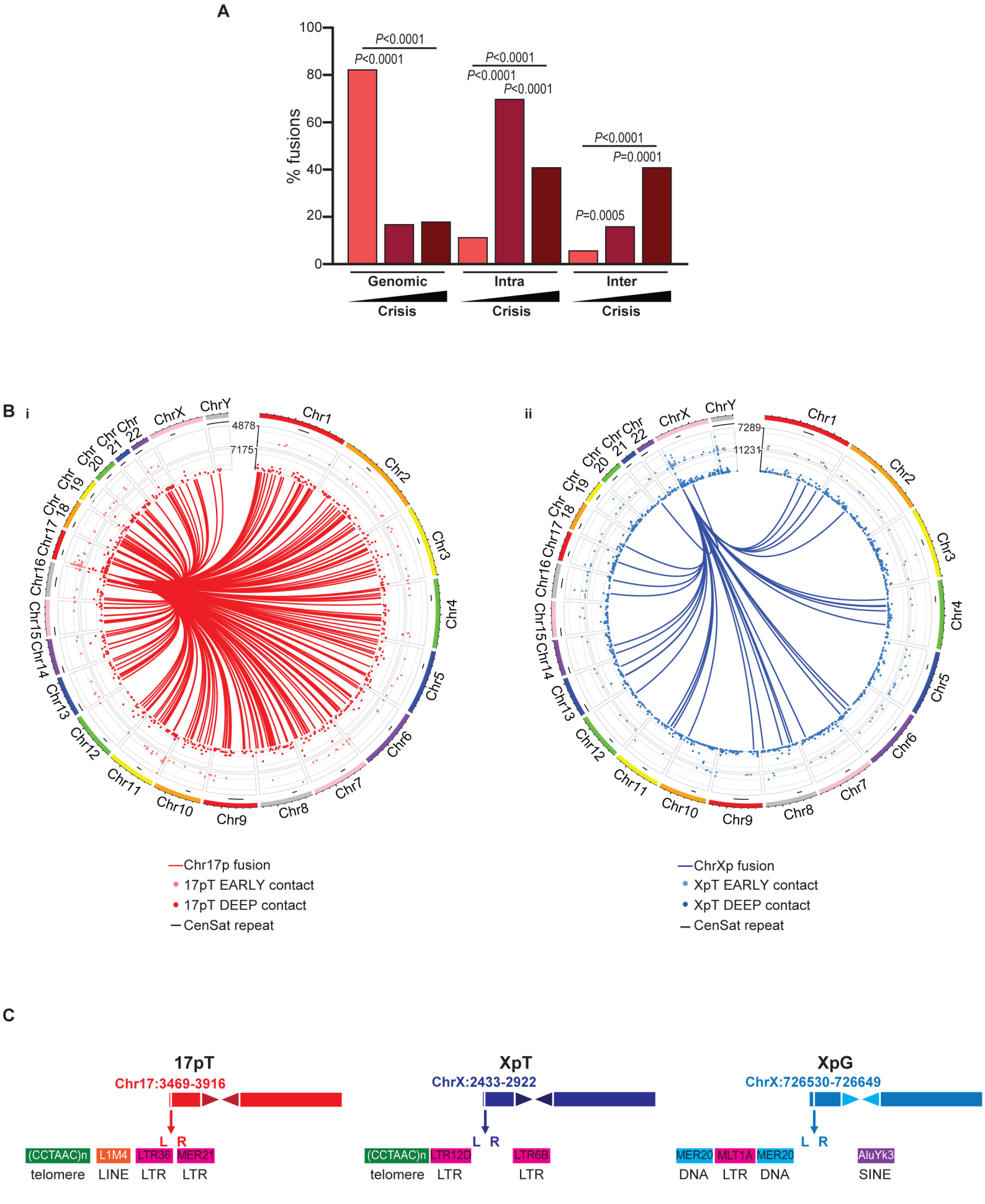
A
% fusions
100
80
60
40
20
0
P<0.0001
P<0.0001
P<0.0001
P<0.0001
P<0.0001
P<0.0001
P=0.0005
P=0.0001
Genomic
Intra
Inter
Crisis
Crisis
Crisis
B i
ii
Chr1
Chr2
Chr3
Chr4
Chr5
Chr6
Chr7
Chr8
Chr9
Chr10
Chr11
Chr12
Chr13
Chr14
Chr15
Chr16
Chr17
Chr 18
Chr 19
Chr 20
Chr 21
Chr 22
ChrX
ChrY
4878
7175
7289
11231
Chr17p fusion
17pT EARLY contact
17pT DEEP contact
CenSat repeat
ChrXp fusion
XpT EARLY contact
XpT DEEP contact
CenSat repeat
C
17pT
Chr17:3469-3916
L R
(CCTAAC)n
telomere
L1M4
LINE
LTR36
LTR
MER21
LTR
XpT
ChrX:2433-2922
L R
(CCTAAC)n
telomere
LTR12D
LTR
LTR6B
LTR
XpG
ChrX:726530-726649
L R
MER20
DNA
MLT1A
LTR
MER20
DNA
AluYk3
SINE

Figure 4

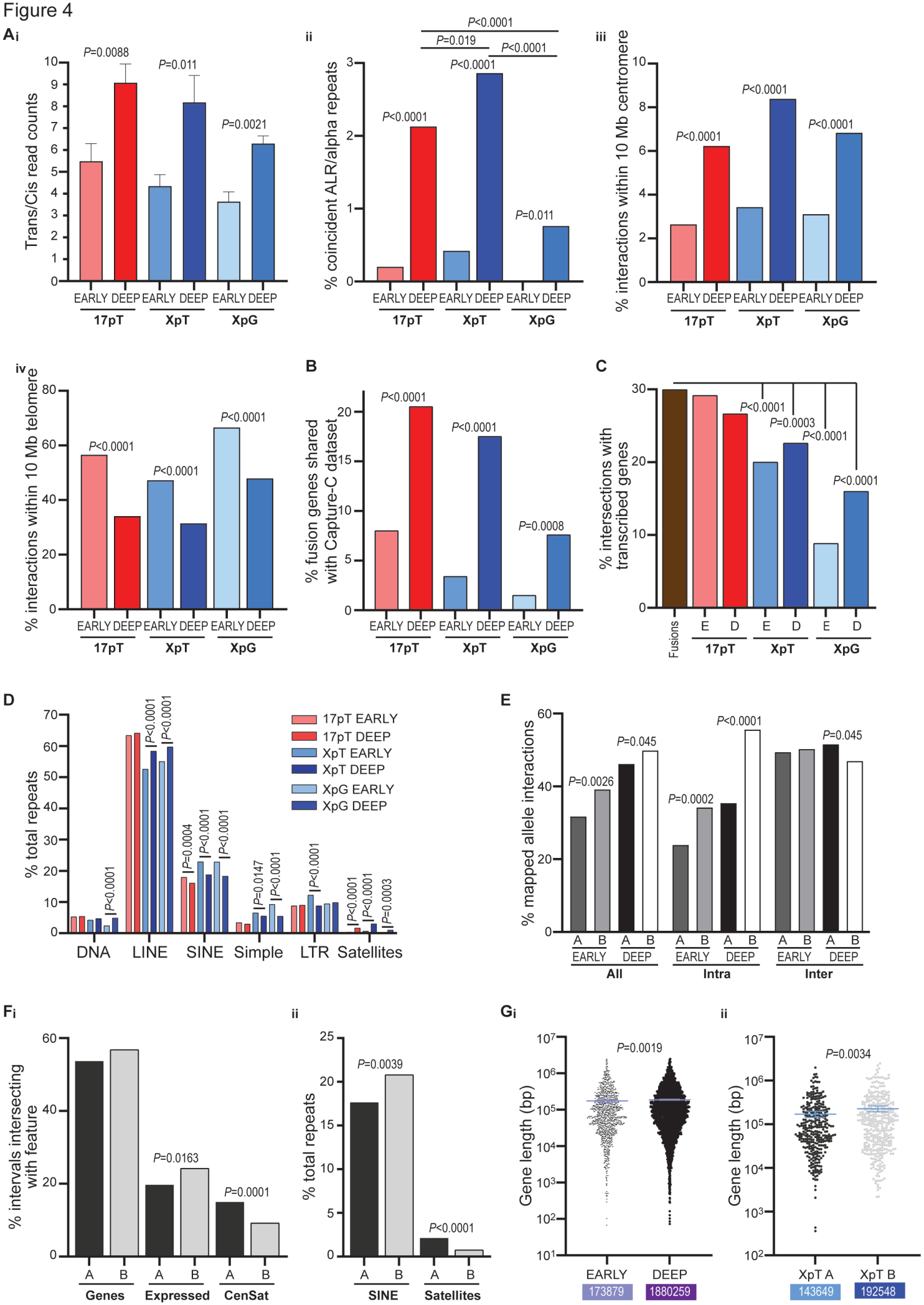
Ai
Trans/Cis read counts
P=0.0088
P=0.011
P=0.0021
EARLY DEEP EARLY DEEP EARLY DEEP
17pT XpT XpG
ii
% coincident ALR/alpha repeats
P<0.0001
P=0.019
P<0.0001
P<0.0001
P<0.0001
P=0.011
iii
% interactions within 10 Mb centromere
P<0.0001
P<0.0001
P<0.0001
iv
% interactions within 10 Mb telomere
P<0.0001
P<0.0001
P<0.0001
B
% fusion genes shared with Capture-C dataset
P<0.0001
P<0.0001
P=0.0008
C
% intersections with transcribed genes
P<0.0001
P=0.0003
P<0.0001
P<0.0001
Fusions E D E D E D
D
% total repeats
17pT EARLY
17pT DEEP
XpT EARLY
XpT DEEP
XpG EARLY
XpG DEEP
DNA LINE SINE Simple LTR Satellites
E
% mapped allele interactions
P=0.0026
P=0.045
P<0.0001
P=0.0002
P=0.045
A B A B A B A B A B A B
EARLY DEEP EARLY DEEP EARLY DEEP
All Intra Inter
Fi
% intervals intersecting with feature
P=0.0163
P=0.0001
A B A B A B
Genes Expressed CenSat
ii
% total repeats
P=0.0039
P<0.0001
A B A B
SINE Satellites
Gi
Gene length (bp)
P=0.0019
EARLY DEEP
173879 1880259
ii
Gene length (bp)
P=0.0034
XpT A XpT B
143649 192548

Figure 5

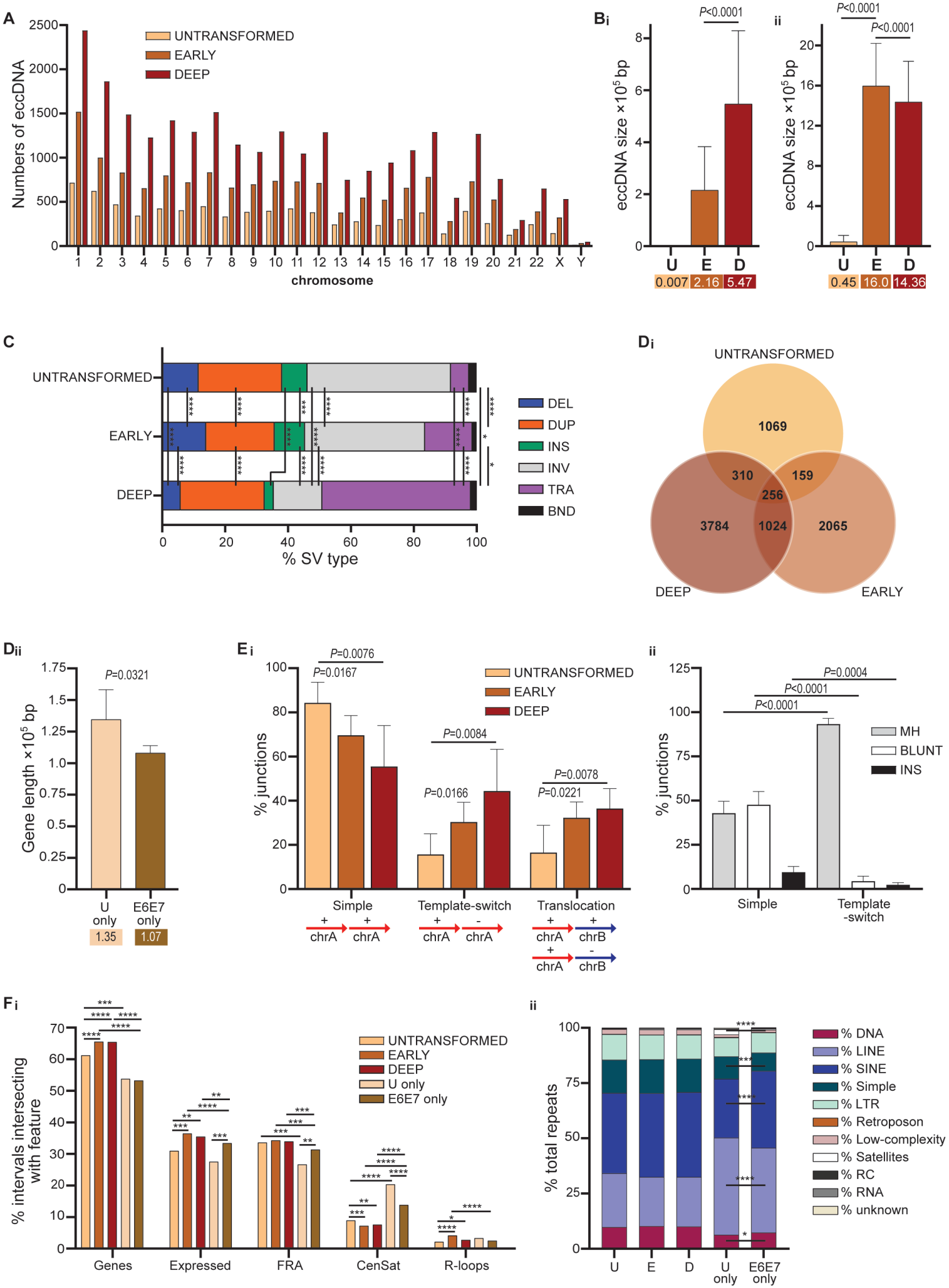
A
Numbers of eccDNA
UNTRANSFORMED
EARLY
DEEP
chromosome
Bi
eccDNA size ×10^5 bp
P<0.0001
U E D
0.007 2.16 5.47
ii
P<0.0001
P<0.0001
P<0.0001
0.45 16.0 14.36
C
UNTRANSFORMED
EARLY
DEEP
DEL
DUP
INS
INV
TRA
BND
% SV type
Di
UNTRANSFORMED
1069
310
159
256
3784
1024
2065
DEEP
EARLY
Dii
Gene length ×10^5 bp
P=0.0321
U only
E6E7 only
1.35
1.07
Ei
% junctions
P=0.0076
P=0.0167
P=0.0084
P=0.0166
P=0.0078
P=0.0221
Simple
Template-switch
Translocation
chrA
chrB
ii
% junctions
P=0.0004
P<0.0001
P<0.0001
MH
BLUNT
INS
Simple
Template -switch
Fi
% intervals intersecting with feature
UNTRANSFORMED
EARLY
DEEP
U only
E6E7 only
Genes
Expressed
FRA
CenSat
R-loops
ii
% total repeats
% DNA
% LINE
% SINE
% Simple
% LTR
% Retroposon
% Low-complexity
% Satellites
% RC
% RNA
% unknown
U
E
D
U only
E6E7 only

Figure 6

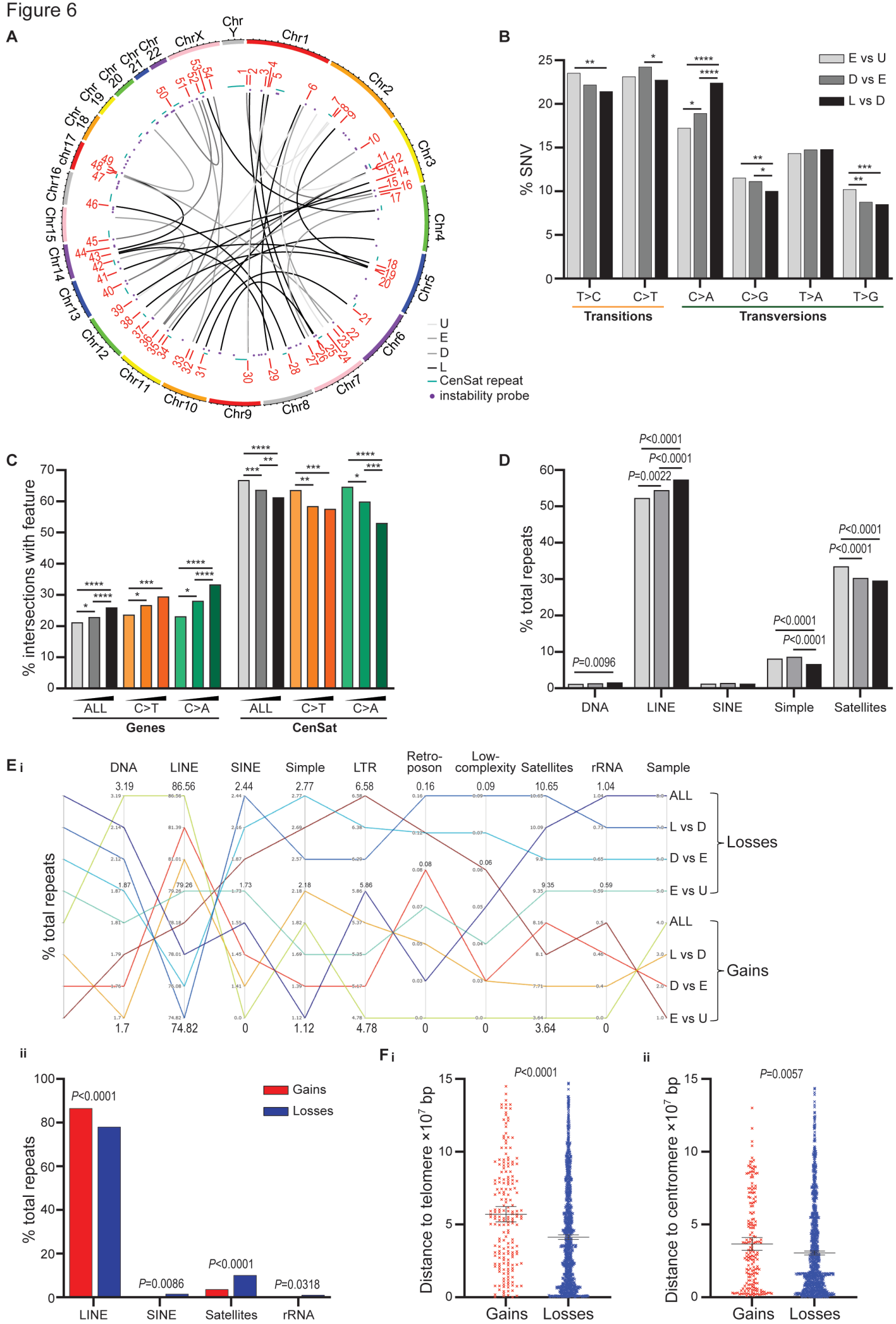
A
Chr Y
ChrX
Chr1
Chr2
Chr3
Chr4
Chr5
Chr6
Chr7
Chr8
Chr9
Chr10
Chr11
Chr12
Chr13
Chr14
Chr15
Chr16
chr17
Chr 18
Chr 19
Chr 20
Chr 21
Chr 22
U
E
D
L
CenSat repeat
instability probe
B
% SNV
E vs U
D vs E
L vs D
T>C
C>T
C>A
C>G
T>A
T>G
Transitions
Transversions
C
% intersections with feature
ALL
C>T
C>A
Genes
CenSat
D
% total repeats
P=0.0096
P=0.0022
P<0.0001
DNA
LINE
SINE
Simple
Satellites
E i
DNA
LINE
SINE
Simple
LTR
Retro-poson
Low-complexity
Satellites
rRNA
Sample
3.19
86.56
2.44
2.77
6.58
0.16
0.09
10.65
1.04
ALL
L vs D
D vs E
E vs U
Losses
Gains
1.7
74.82
0
1.12
4.78
0
0
3.64
0
% total repeats
ii
P<0.0001
P=0.0086
P<0.0001
P=0.0318
LINE
SINE
Satellites
rRNA
Gains
Losses
F i
P<0.0001
Distance to telomere ×10^7 bp
Gains
Losses
ii
P=0.0057
Distance to centromere ×10^7 bp
Gains
Losses